bioRxiv preprint doi: https://doi.org/10.1101/2023.01.23.524173; this version posted January 23, 2023. The copyright holder for this preprint (which was not certified by peer review) is the author/funder. All rights reserved. No reuse allowed without permission.

1

2 # Global analysis of aging-related protein structural changes
3 # uncovers enzyme polymerization-based control of longevity

4 **Authors:** Jurgita Paukštytė[1,2], Rosa María López Cabezas[1,2], Yuehan Feng[3], Kai Tong[1,2,4,5],
5 Daniela Schnyder[3], Ellinoora Elomaa[1,2], Pavlina Gregorova [2], Matteo Doudin[1,2], Meeri
6 Särkkä[1,2], Jesse Sarameri[1,2], Alice Lippi[6], Helena Vihinen[7], Juhana Juutila[2,7], Anni
7 Nieminen[2,7], Petri Törönen[2,7], Liisa Holm[2,7], Eija Jokitalo[7], Anita Krisko[6], Juha Huiskonen[7],
8 L. Peter Sarin[2], Ville Hietakangas[2,7], Paola Picotti[3,8], Yves Barral[3], Juha Saarikangas[1,2,7,9,*]
9
10 **Affiliations:** [1]Helsinki Institute of Life Science, HiLIFE, University of Helsinki; Helsinki,
11 Finland. [2]Faculty of Biological and Environmental Sciences University of Helsinki; Helsinki,
12 Finland. [3]Institute of Biochemistry, ETH Zurich; Zurich, Switzerland. [4]School of Biological
13 Sciences, Georgia Institute of Technology; Atlanta, Georgia, United States. [5]Interdisciplinary
14 Graduate Program in Quantitative Biosciences, Georgia Institute of Technology; Atlanta,
15 Georgia, United States. [6]Department of Experimental Neurodegeneration, University Medical
16 Center Göttingen; Göttingen, Germany. [7]Institute of Biotechnology, HiLIFE, University of
17 Helsinki; Helsinki, Finland. [8]Institute of Molecular Systems Biology, ETH Zurich; Zurich,
18 Switzerland. [9]Neuroscience Center, HiLIFE, University of Helsinki; Helsinki, Finland.

19 *Correspondence: juha.saarikangas@helsinki.fi

20

21 **Abstract:**
22 Aging is associated with progressive phenotypic changes over time. Virtually all cellular
23 phenotypes are produced by proteins and structural alterations in proteins can lead to age-related
24 diseases. Nonetheless, comprehensive knowledge of proteins undergoing structural-functional
25 changes during cellular aging and their contribution to age-related phenotypes is lacking. Here, we
26 conducted proteome-wide analysis of early age-related protein structural changes in budding yeast
27 using limited proteolysis-mass spectrometry. The results, compiled in online ProtAge-catalog,
28 unravelled age-related functional changes in regulators of translation, protein folding and amino
29 acid metabolism. Mechanistically, we found that folded glutamate synthase Glt1 polymerizes into
30 supramolecular self-assemblies during aging causing breakdown of cellular amino acid
31 homeostasis. Inhibiting Glt1 polymerization by mutating the polymerization interface restored
32 amino acid levels in aged cells, attenuated mitochondrial dysfunction and led to life span
33 extension. Altogether, this comprehensive map of protein structural changes enables identifying
34 novel mechanisms of age-related phenotypes and offers opportunities for their reversal.
35

36
37

bioRxiv preprint doi: https://doi.org/10.1101/2023.01.23.524173; this version posted January 23, 2023. The copyright holder for this preprint (which was not certified by peer review) is the author/funder. All rights reserved. No reuse allowed without permission.

38 **Main Text:**

39 ## Introduction

40 The three-dimensional structures of proteins define how genetic information is translated into
41 cellular biochemistries. As such, structural information of proteins is required to fully comprehend
42 how cellular and organismal phenotypes arise [1–4]. Most proteins can occupy various structural
43 states in different contexts. Variation can result, for example, from interactions with other
44 molecules [5,6], post-translational modifications [7], fold switching [8], unstructured regions [9,10] and
45 condensation-reactions [11,12]. However, at present we know little of the diversity and dynamics of
46 protein structural variation and even less about how it contributes to phenotypic diversity of cells
47 and organisms.

48 Aging is a nearly universal biological process characterized by progressive phenotypic changes
49 and increased mortality over time [13,14]. The rate of these changes is influenced by genetic variance,
50 life history and environment. These variables can be experimentally controlled in model
51 organisms, allowing for a more precise investigation of the mechanisms underlying aging
52 phenotypes. For instance, the single-celled organism *Saccharomyces cerevisiae* starts to
53 systematically display aging phenotypes during early stages of replicative aging that are not caused
54 by mutations [15–17]. Such phenotypes include evolutionarily conserved aging hallmarks such as
55 changes in cellular size [18], metabolism [19,20], organelle function [21–23] and the formation of protein
56 aggregates [24,25]. Understanding how these and other phenotypic changes in aging arise can lead to
57 the discovery of early causal mechanisms of cascading negative effects and thereby provide
58 opportunities for interventions.

59 It is still not clear what gives rise to progressive phenotypic changes in aging. The prevailing theory
60 is that molecular damage, for example due to free radicals [13,26] in conjunction with changes in the
61 fidelity of epigenetic modifications [27], transcription [28,29], translation [30–32] and metabolism [19],
62 contributes to physiological changes in aging. In addition, aging is associated with alterations in
63 the abundance, turnover or folding of proteins that are typically linked to defective protein
64 homeostasis [33–35]. Folding changes in turn can lead to protein aggregation, which is a shared feature
65 of aging across organisms and tissue types [36,37], and is infamously linked to age-related
66 neurodegenerative diseases [38]. However, it is currently unclear whether cellular aging results in
67 other types of protein structural changes beyond aggregation. Thus, a more comprehensive
68 characterization of protein structural states is required to understand the full breadth of proteome
69 activity changes during aging and their contribution to adaptive and maladaptive age-related
70 phenotypes.

71

72 ## Results

73 ### *Global analysis of aging-associated structural changes*

74 To identify aging-associated structural changes on a proteome-wide scale, we used magnetic-
75 activated affinity purification to obtain fractions of young (av. age 0.6 divisions ±0.91 STD) and
76 aged (av. age 4.2 divisions ±0.65 STD) budding yeast cells (**Fig. 1A**). Yeast cells aged for an
77 average of 4.2 divisions represents mother cells that begin to systematically display aging
78 phenotypes that are not caused by mutations [15–17], enabling us to capture the underlying processes
79 behind these age-related changes as they emerge. Such phenotypes include conserved aging
80 hallmarks such as the appearance of protein aggregates and the declined function of organelles
81 such as mitochondria and vacuoles [21,22,25]. The young cells represent rejuvenated daughter cells

bioRxiv preprint doi: https://doi.org/10.1101/2023.01.23.524173; this version posted January 23, 2023. The copyright holder for this preprint (which was not certified by peer review) is the author/funder. All rights reserved. No reuse allowed without permission.

82 (since aging factors are retained in the mother cell) [15–17,39]. We extracted native proteomes from
83 young and aged cells, subjected them to limited proteolysis (LiP) via brief proteinase K treatment,
84 followed by denaturation, trypsin digestion and mass spectrometry analysis (LiP-MS) [40,41]. A
85 consequence of LiP is that protein structural features impact the cleavage patterns, enabling
86 identification of age-related structural alterations in proteins at peptide-level resolution (**Fig. 1A**).
87 To normalize the LiP-MS results for age-related changes in protein abundance, the same samples
88 were also analyzed without the LiP step.
89
90 We considered that proteins with significant differences in proteolytic cleavage patterns
91 normalized to their abundance between young and aged cells have undergone an aging-related
92 structural change (collectively referred to hereafter as *age-altered proteins*) (**Fig. 1A**). LiP-MS
93 enables reproducible identification of structural changes caused for example by alterations in
94 protein folding, assembly state, interaction with other molecules or post-translational
95 modifications, thereby offering a readout for age-associated changes in protein function [3,40,42].
96
97 The global comparison of protein structural states between young and aged cells uncovered age-
98 dependent structural differences in 468 proteins that comprised 1272 conformation-specific
99 peptides (fold change q-value < 0.05 from sample triplicates, total proteins detected: 2833) (**Fig.
100 1A**). These conformotypic peptides identify the protein regions that changed structure during early
101 aging. We mapped all structurally altered regions to their Alpha Fold-predicted three dimensional
102 (3D) protein structures [43] and collected these results together with other relevant features into the
103 online ProtAge-catalog (https://protage-server-21.it.helsinki.fi/) (**Fig. S1A)**.
104
105 To uncover shared features of age-altered proteins, we compared the structurally altered proteome
106 to the detected proteome that did not show significant structural changes (*unaltered proteins*). We
107 found that age-altered proteins had on average more assigned gene ontology (GO) terms and
108 protein-protein interactions, suggesting that these proteins are pleiotropic and participate in diverse
109 cellular functions (**Fig. 1B-C, Fig. S1B**). GO enrichment analyses showed that regulators of
110 metabolism, translation, protein folding and oxidative stress responses were overrepresented in the
111 age-altered proteome (p.adj < 0.05 **Fig. 1D**). The age-altered proteins contained a larger fraction
112 of essential genes and had a lower mutation rate than the unaltered proteins (**Fig. S1C-D**).
113 Interestingly, even though the distribution of protein solubility was similar between age-altered
114 proteins and the unaltered proteins (**Fig. S1E**), there was a strong enrichment for proteins that can
115 transition into biomolecular condensates during stress [44], including stress granule components
116 (**Fig. 1E-F**). Moreover, age-altered proteins were strongly enriched in a class of long-lived proteins
117 that are retained in the aging mother cells, suggesting that their retention is associated with an
118 underlying structural change [45] (**Fig. 1G**). In addition to being long-lived, the age-altered proteins
119 were more abundant than the unaltered proteins, which could be explained by the overall higher
120 translation rate and lower number of degradation signals in these proteins (**Fig. S1F-H**). Finally,
121 we found that decreased expression of genes encoding for the age-altered proteins in budding yeast
122 or their homologs in *Caenorhabditis elegans* were more readily associated with life span extension
123 as compared to the genes encoding for the unaltered proteins (**Fig. 1H**). Taken together, aging-
124 associated structural changes are prevalent in pleiotropic regulators of metabolism, growth and
125 stress responses that can transition between soluble and assembled states during stress.
126
127 ***Structural changes identify activity changes in regulators of protein homeostasis***
128 Can the structural changes provide new insights in protein function during aging? We observed
129 significant structural changes in all major chaperone classes, including members of Hsp40, Hsp70,

bioRxiv preprint doi: https://doi.org/10.1101/2023.01.23.524173; this version posted January 23, 2023. The copyright holder for this preprint (which was not certified by peer review) is the author/funder. All rights reserved. No reuse allowed without permission.

130 Hsp90, Hsp100, Hsp110 and TRiC/CCT proteins, which are interconnected and implicated in the
131 maintenance of proteostasis during aging **(Fig. S2A)** [33,34,46]. The major Hsp70 isoform Ssa1
132 availability is compromised during aging [47], but how this decline in function relates to structure is
133 unclear. To address this question, we mapped the structurally altered regions in Ssa1. Intriguingly,
134 they clustered around two major sites undergoing activity-dependent structural changes during the
135 Hsp70 allosteric cycle: the nucleotide binding domain (NBD) and the substrate binding domain
136 (SBD) [48] (**Fig. 2A, Fig. 2B**). Moreover, all three full tryptic peptides localizing to the SBD showed
137 significantly increased abundance in the aged cells as compared to young cells, suggesting that
138 this region in SBD (residues 413-447) was less accessible for proteolytic cleavage in aged cells
139 (**Fig. 2A**). To investigate whether the reduced accessibility of SBD reflects increased occupancy
140 by clients, we performed a contact-site analysis using the substrate bound structure of bacterial
141 Hsp70 DnaK. The proteolytically protected regions overlapped with the evolutionarily conserved
142 residues that mediate critical hydrogen bonding and hydrophobic interactions with the clients [49,50]
143 (**Fig. 2B**). These data are consistent with the increased client-binding of Ssa1 in aged cells, as
144 previously measured by a decreased diffusion coefficient [47] and increased association with protein
145 aggregates [25] (**Fig. 2C**). The results therefore provide validation of the ability of the LiP-MS
146 approach to identify relevant aging-associated proteomic changes. Interestingly, the ribosome-
147 associated Hsp70 proteins Ssb1 and Ssb2 and the endoplasmic reticulum Kar2/BiP showed a
148 similar pattern of structural alterations in the SBD regions that overlapped with the client-binding
149 site [49,50] (**Fig. S2C-H**), suggesting that aging might also lead to increased client occupancy of
150 Hsp70s that govern nascent protein folding in cytoplasm and ER, respectively. Overall, we propose
151 that the observed structural changes in Hsp70 proteins reflect an overall age-related increase in
152 client occupancy, and this change may impact the proteostasis of cytosolic and ER residing
153 proteins.
154
155 One cause of compromised proteostasis during aging is altered protein translation accuracy [31,32].
156 Indeed, age-altered proteins were enriched in proteins regulating translation and tRNA
157 aminoacylation and included some tRNA modifying enzymes (**Fig. 1D**). tRNA modifications
158 regulate the kinetics and accuracy of translating ribosomes and thereby contribute to protein
159 folding [51]. However, it is unknown whether specific tRNA modifications change during aging. We
160 noticed that Trm1, which catalyzes N2,N2-dimethylguanosine ($m^{2,2}G$) modification at a position
161 G_{26} in tRNAs, undergoes an age-related structural change that localized to the conserved Motif II
162 (**Fig. 2D**). This motif is part of the methyl donor molecule binding pocket that is important for
163 Trm1 catalytic activity. Contact site analysis revealed that the LiP-peptide directly overlaps with
164 S-adenosyl-l-methionine (AdoMet) binding site and included the conserved Asp78 that mediates
165 hydrophilic interaction with the ribose group of AdoMet [52] (**Fig. 2D-E, Fig. S3A**). The
166 modification site specificity of Trm1 on tRNAs (**Fig. S3B**) enabled us to test whether the observed
167 structural change corresponds to an activity change during aging. For this, we extracted tRNAs
168 from young and aged cells and quantified the $m^{2,2}G$ modification by mass spectrometry.
169 Interestingly, we found a significantly increased abundance of $m^{2,2}G$ in aged cells (**Fig. 2F**),
170 consistent with increased occupancy of Trm1 active site in aged cells.
171
172 Overall, we found structural changes in key proteins regulating proteostasis at the level of
173 translation and folding, consistent with age-related increased substrate association. More
174 generally, these results underline that LiP-MS can facilitate identification of specific age-related
175 functional changes in proteins and guide their mechanistic analysis.
176
177 ***Glutamate synthase Glt1 transitions to mesoscale assemblies during aging***

bioRxiv preprint doi: https://doi.org/10.1101/2023.01.23.524173; this version posted January 23, 2023. The copyright holder for this preprint (which was not certified by peer review) is the author/funder. All rights reserved. No reuse allowed without permission.

178 Amino acid metabolizing enzymes were the most overrepresented class of age-altered proteins
179 (**Fig. 1D and SFig. 4A**). To evaluate if the structural changes impact function, we chose to examine
180 whether age-altered metabolic enzymes show changes in subcellular localization or organization,
181 we used fluorescence microscopy to visualize GFP-tagged versions of endogenous cytoplasmic
182 amino acid synthesizing enzymes in young and aged cells. Most enzymes showed diffuse
183 cytoplasmic localization with no detectable age-related changes (**Fig. S4B**). A subset of enzymes
184 showed a punctate pattern, which in some cases appeared to be associated with localization to
185 organelles (**Fig. S4C**). Intriguingly, unlike all other proteins in this class, the glutamate synthase
186 Glt1 displayed a clear and systematic age-related localization change: in young cells Glt1 was
187 diffusely distributed throughout the cytoplasm, but in aged cells that had undergone 4-6 divisions
188 Glt1 had transitioned into large rod-shaped structures, which we show below are Glt1 polymers
189 (**Fig. 3A-B, Fig. S4C, Movie S1**). The Glt1 polymers formed in a similar manner when tagged
190 with either GFP or monomeric mKate2 fluorophores (**Fig. S4D**).
191
192 Metabolic enzymes, including Glt1, were previously observed to form polymers in energy-starved,
193 non-cycling cells [53–56]. The Glt1 structures resembled these polymers. However, the aged cells
194 carrying Glt1 polymers were cycling normally (**Movie S1**). Live-cell imaging further revealed that
195 Glt1 polymers were retained in the aging mother cells during cell division, and the daughter cells
196 were born with diffuse Glt1 (**Fig. 3C, Movie S1**). The timing of appearance and mitotic
197 segregation pattern of Glt1 assemblies resembled that of aging-associated aggregates [25,47].
198 However, Glt1-GFP polymers did not colocalize with Hsp104-labelled aggregates (**Fig. S4E**),
199 indicating that Glt1 polymers do not have features of canonical aggregates.
200
201 As Glt1 polymers did not appear to be aggregates, we investigated how their formation is
202 regulated. We tested if Glt1 polymerization responds to availability of key nutrients by modulating
203 the levels of glucose, nitrogen and amino acids. Interestingly, we found that Glt1 polymerization
204 was affected by amino acid availability but not by limiting glucose or nitrogen (**Fig. 3D, Fig. S5A-**
205 **B**). Incubating cells in growth medium lacking amino acids inhibited Glt1 polymer formation
206 during replicative aging, whereas the addition of minimal amino acids for growth, methionine,
207 histidine and leucine (minimal media, MM) was sufficient to restore polymer formation (**Fig. 3D**).
208 Polymer formation was further increased by adding peptone as the source for all amino acids, or
209 by using synthetic complete (SC) media, that contains most amino acids (see methods for details)
210 (**Fig. 3D**). These data suggest that Glt1 polymerization during aging is a tunable reaction that is
211 regulated by amino acid levels.
212
213 To test if Glt1 polymers are reversible and can depolymerize, we used microfluidics-coupled live
214 cell imaging and quantified the fate of preexisting Glt1 polymers upon acute removal of amino
215 acids. Indeed, switching aged cells from rich SC media to amino acid-deprived media caused a
216 systematic and progressive depolymerization of Glt1 polymers (**Fig. 3E-F**). Thus, Glt1
217 polymerization in aged cells is reversible.
218
219 ***Glt1 polymerizes through self-association of symmetric complexes***
220 To understand the nature of the Glt1 structures, we examined them using correlative light and
221 transmission electron microscopy (CLEM). Importantly, the electron micrographs showed that the
222 Glt1 polymers are composed of bundled filaments (**Fig. 3G**). This filamentous ultrastructure
223 suggested that Glt1 assembly might occur at the polymer ends. To test this, we compiled a live-
224 cell imaging assay to follow the fusion of two mating yeast cells carrying GFP- or mKate2-tagged
225 versions of Glt1. By following the fate of distinct Glt1 polymers in the newly formed zygote, we

bioRxiv preprint doi: https://doi.org/10.1101/2023.01.23.524173; this version posted January 23, 2023. The copyright holder for this preprint (which was not certified by peer review) is the author/funder. All rights reserved. No reuse allowed without permission.

226 found that the two polymers were able to join at their distal ends in a stable manner, providing
227 evidence that the Glt1 polymers can grow at the tips through the addition of new subunits (**Fig.**
228 **3H**). To gain more insight into the polymerization dynamics, we measured polymer growth in
229 individual cells over several hours (**Fig. 3I**). Fitting 76 polymer growth traces starting from their
230 nucleation (distinguished as the first visible Glt1-GFP puncta) revealed a bi-phasic growth curve.
231 In the initial 24-minute fast-growing state the doubling time of polymer elongation was 7.9
232 minutes, which was followed by a 22-times slower growth phase (**Fig. 3J**). Together, these data
233 indicate that Glt1 undergoes a rapid switch-like transition from diffuse to filamentous polymers
234 during the early aging of budding yeast cells.
235
236 To understand the structural basis of Glt1 polymerization, we modelled the yeast Glt1 structure
237 based on the structure of the homologous *Azospirillum brasilense* GltS, which consists of two
238 subunits that assemble into a hexameric oligomer with threefold dihedral (D3) symmetry [57]. We
239 found that the three LiP-MS identified Glt1 peptides that were protected from proteolytic cleavage
240 in aged cells localized on the three-fold symmetric face of the GltS structure (**Fig. 3K**). We
241 hypothesized that this face represents the polymerization interface mediating Glt1 self-assembly
242 and becomes protected from proteolytic cleavage when Glt1 is polymerized. To test this
243 hypothesis, we performed site-directed mutagenesis focusing on the LiP-MS identified region (LiP
244 1). Surface hydrophobicity can mediate the self-assembly of symmetric protein complexes [58], and
245 we found that exchanging surface exposed hydrophobic residues for polar residues compromised
246 Glt1 polymerization during aging (**Fig. 3L-M, Fig. S5C**). We focused on mutant 3 (H1537A,
247 Y1538N, L1539S, henceforth *GLT1-MUT*) and validated that it displayed similar expression and
248 catalytic activity as wild type Glt1 (**Fig. S5D-G**), demonstrating that the mutation does not prevent
249 polymerization through adverse effects on Glt1 expression or folding. Overall, our data suggest
250 that Glt1 filaments form during aging via the polymerization of hexameric (D3 symmetry) or
251 trimeric (cyclic, C3 symmetry) Glt1 homomers (**Fig. 3N, Fig. S5H-I**).
252
253 ***Inhibiting Glt1 polymerization delays aging, prevents intracellular amino acid accumulation***
254 ***and attenuates mitochondrial dysfunction***
255 Several metabolic enzymes undergo reversible polymerization as an adaptive response to changes
256 in the environment [59,60]. We considered whether age-related Glt1 polymerization is an adaptation
257 that impacts cellular longevity. To test this, we compared the replicative life span of wild type cells
258 to that of CRISPR-Cas9-edited cells expressing non-polymerizing *GLT1-MUT*. Interestingly,
259 microdissection mediated life span analysis revealed that the polymerization-deficient *GLT1-MUT*
260 cells displayed a 20 % extension in median life span as compared to the wild type cells ($p < 0.05$,
261 **Fig. 4A**). These data suggest that the Glt1 transition from the diffuse to polymerized form may
262 promote aging in yeast cells.
263
264 To understand the role of Glt1 polymerization in aging and overall cellular function, we first
265 compared the transcriptome of young and aged wild type and *GLT1-MUT* cells using RNA
266 sequencing (**Fig. 4B**). We observed 814 genes with altered expression in aged wild-type versus
267 *GLT1-MUT* cells, whereas the expression of only 11 genes was altered between young cells where
268 Glt1 is soluble (**Fig. S6A**). Gene set enrichment analysis of the 814 genes showed significant
269 differences in metabolic processes, with amino acid metabolism representing the second most
270 significant GO-category (**Fig. S6B**). Together with the sensitivity of Glt1 polymerization to amino
271 acid levels, this suggested that the Glt1 polymerization status is coupled to amino acid metabolism.
272 We explored this further via targeted LC-MS metabolic analyses of young and aged wild type and
273 *GLT1-MUT* cells (**Fig. 4B**). Principal component analysis (PCA) of the steady-state metabolome

bioRxiv preprint doi: https://doi.org/10.1101/2023.01.23.524173; this version posted January 23, 2023. The copyright holder for this preprint (which was not certified by peer review) is the author/funder. All rights reserved. No reuse allowed without permission.

274 showed that aged wild-type cells clustered away from young wild-type cells, indicating that aging
275 correlates with changes in cellular metabolism (**Fig. 4C**). Interestingly, aged wild-type cells
276 carrying Glt1 polymers were the most distal cluster from the young cells and segregated away
277 from the aged *GLT1-MUT* cells, indicating that aged yeast cells with Glt1 polymers have a distinct
278 metabolic phenotype. Notably, young wild-type and *GLT1-MUT* samples co-clustered (**Fig. 4C**),
279 which, together with the RNA seq data (**Fig. S6A**), further demonstrate that the H1537A, Y1538N,
280 L1539S substitutions affect polymerization but do not alter the function of soluble Glt1.
281
282 We examined metabolites by performing an orthogonal partial least square (OPLS) analysis and
283 observed increased amino acid levels and reduced mitochondrial TCA cycle metabolites in aged
284 wild-type cells relative to aged *GLT1-MUT* cells (**Fig. 4D-E**). Indeed, the steady-state levels of
285 amino acids increased up to 7-fold during aging in wild-type cells but not in *GLT1-MUT* cells (**Fig.**
286 **4F**). We confirmed that these differences cannot be explained by changes in cell size between the
287 wild type and mutant cells (**Fig. S7A**). It was recently shown that loss of vacuolar acidification
288 leads to overflow of cytosolic amino acids in aged yeast cells [22,61]. We found that 8 out of 14 of
289 vacuolar V-ATPase subunits displayed a structural change during aging, in line with a potential
290 change in its function during aging. Thus, we tested if Glt1 polymerization is associated with
291 vacuolar decline. However, Glt1 polymerization status did not affect vacuolar pH (**Fig. S7B**).
292 Furthermore, inhibiting vacuolar ATPase with concanamycin A (ConcA) did not induce Glt1
293 polymerization (**Fig. S7C**). We conclude that Glt1 polymerization-associated increase in
294 cytoplasmic amino acids is not associated with vacuolar decline.
295
296 To understand the origin of the increased amino acids, we performed a tracing analysis, growing
297 cells with $^{13}C_5$-$^{15}N_2$ isotope-labelled glutamine for 30 min **(Fig. 4B)**. Glt1 catalyzes the transfer of
298 one amino group from a glutamine molecule to alpha-ketoglutarate, generating two glutamate
299 molecules while NADH is oxidized in the process (**Fig. 4G**). We thus quantified the fraction of
300 labelled glutamate derived from the Glt1 reaction relative to the rest of the labelled glutamate
301 species derived from the Gdh1 and Gdh3 reactions. We found no differences in labelled glutamate
302 levels between young and aged wild type or *GLT1-MUT* cells (**Fig. 4H, Fig. S7E-F**), suggesting
303 that Glt1 retains its catalytic activity when it is polymerized. However, we observed that glutamine
304 uptake was significantly increased in aged wild-type cells that carried Glt1 polymers (**Fig. 4I, Fig.**
305 **S7E, G**).
306
307 These results suggested that the increase in amino acid levels may be mediated via differential
308 uptake of glutamine and possibly other amino acids. Indeed, our RNA-seq identified amino acid
309 transporters as a significantly altered GO-cluster between aged wild-type and *GLT1-MUT* cells (p
310 adj.< 0.05) (**Fig. S6B**). To test whether increased glutamine import is linked to increased
311 expression of glutamine transporters, we measured the expression of broad-specificity amino acid
312 transporters Gnp1, Dip5 and Gap1 in young and aged wild-type and *GLT1-MUT* cells.
313 Interestingly, Gnp1 and Dip5 displayed approximately 2-fold higher protein expression in the aged
314 wild-type as compared to *GLT1-MUT* cells whereas no changes were detected in Gap1 (**Fig. S8A**).
315 Gnp1 has high affinity for glutamine [62]. In accordance with our metabolic analysis, we found that
316 the expression of Gnp1 increased with age, and its levels in wild-type cells were significantly
317 higher than in *GLT1-MUT* cells (**Fig. S8B-C**). We propose that Glt1 polymerization contributes to
318 increased expression of amino acid transporters, including Gnp1, to promote the uptake of
319 glutamine and likely other amino acids in aged cells (**Fig. 4J**).
320

bioRxiv preprint doi: https://doi.org/10.1101/2023.01.23.524173; this version posted January 23, 2023. The copyright holder for this preprint (which was not certified by peer review) is the author/funder. All rights reserved. No reuse allowed without permission.

321 Aged cells showed an accumulation of many amino acids (**Fig. 4F**). Since glutamine can serve as
322 an amino group donor for the synthesis of other amino acids, we examined whether aged cells
323 utilize excess glutamine to synthesize other amino acids **(Fig. S7D)**. Briefly, we used the tracing
324 data to monitor the transfer of the labelled amino group derived from glutamine. Importantly, a
325 comparison of ^{15}N-labelled amino acids between wild-type and *GLT1-MUT* cells showed a
326 significant increase of labelled phenylalanine in aged wild-type cells, but not in aged *GLT1-MUT*
327 cells or young cells (**Fig. 4J**). A similar trend was observed in leucine/isoleucine (**Fig. 4K**). These
328 data provide evidence that Glt1 polymerization-mediated glutamine uptake contributes to the
329 accumulation of other amino acids, particularly phenylalanine. Altogether, these data indicate that
330 Glt1 polymerization is associated to large scale metabolic and transcriptomic rearrangements
331 during aging that lead to amino acid accumulation in aged cells and a shortened life span.
332
333 We therefore wanted to understand how the Glt1 polymerization-associated metabolic
334 rearrangements in aged cells relate to the regulation of longevity. To first understand how Glt1
335 polymerization relates to aging (**Fig. 4A)**, we inspected mortality rates to determine at which
336 timepoint *GLT1-MUT* cells begin to diverge from wild-type cells. We found that *GLT1-MUT*
337 specifically impacted early mortality, in line with the timing of initial polymer formation (**Fig.**
338 **S9A**).
339
340 Mitochondria function begins to decline during early aging in budding yeast [21,22]. Importantly, this
341 decline in mitochondrial function is associated with an overflow of cytosolic amino acids [22,61,63].
342 Thus we measured mitochondrial membrane potential in young and aged cells as a proxy for
343 mitochondrial fitness [64] (**Fig. S9B**), and found that mitochondrial membrane potential declined
344 with age, as expected [21,22] (**Fig. 4L and Fig. S9C**). In contrast, the non-polymerizing *GLT1-MUT*
345 cells maintained high mitochondrial membrane potential during the early phases of aging **(Fig. 4L**
346 **and Fig. S9C**). Moreover, mitochondria were fragmented nearly twice as often in aged wild type
347 cells (9.7 %) as compared to aged *GLT1-MUT* cells (5.1 %) (**Fig. S9D**). We did not detect
348 significant differences in mitochondrial respiration by oxygraphy measurements at this point,
349 probably since most cells are fermenting in these conditions (**Fig. S9E**). We considered an option
350 where the decline in mitochondrial membrane potential could itself act as a signal to promote Glt1
351 polymerization. To test this, we reduced mitochondrial membrane potential by treating cells with
352 carbonyl cyanide m-chlorophenyl hydrazone (CCCP), but this treatment had no effect on Glt1
353 polymerization (**Fig S9F**). The combined data suggest that polymerization does not depend on
354 mitochondrial dysfunction, but that lack of polymerization can counteract mitochondrial
355 dysfunction in aging cells.
356
357 Finally, we addressed the connection between Glt1 polymerization state and mitochondrial
358 decline, testing the role of amino acid accumulation. We measured mitochondrial membrane
359 potential in cells grown under moderate (SD media) and high (SD media + peptone) amino acid
360 conditions that cause an elevation in intracellular amino acids, mimicking the effect of Glt1
361 polymerization in aged cells (**Fig. 4F**). Remarkably, culturing cells in high amino acid conditions
362 reduced mitochondrial membrane potential in all cell populations, abolishing both age- and
363 polymerization-associated differences (**Fig. 4M**). We infer that Glt1 polymerization compromises
364 mitochondrial membrane potential via the elevation of intracellular amino acids.
365
366 **Discussion**
367 Our findings demonstrate that mapping protein structural changes is a powerful way to identify
368 mechanisms associated with cellular aging, which would have not been detectable with prevailing

bioRxiv preprint doi: https://doi.org/10.1101/2023.01.23.524173; this version posted January 23, 2023. The copyright holder for this preprint (which was not certified by peer review) is the author/funder. All rights reserved. No reuse allowed without permission.

369 techniques that only quantify changes in transcriptome and proteome abundance. Since more than
370 80 percent of the structurally altered proteins have human homologs and showed enrichment for
371 genes modulating life span in multicellular *C. elegan*s, the dataset has the potential to be broadly
372 applicable.
373
374 The age-altered proteins identified in this study were enriched in essential, multifunctional proteins
375 that occupied central positions in protein-protein interaction networks. Another interesting feature
376 was the strong enrichment in proteins that can reversibly transition into condensates. Such proteins
377 have emerged as major regulators of adaptive cellular responses that may adopt aberrant
378 conformations during aging and age-related diseases [11,12,65]. A subtype of condensates not
379 previously linked to aging are structurally ordered polymeric assemblies made by metabolic
380 enzymes. We show that surface-exposed hydrophobic residues mediate the self-assembly of
381 symmetric Glt1 homomers during aging. The overall assembly mechanism of Glt1 is similar to
382 that of several other homo-oligomeric proteins with internal symmetry [58,66], suggesting that cell
383 intrinsic alterations in aging might increase the self-association potential of a broader range of
384 proteins. It is not yet clear why aging leads to Glt1 polymerization. We provide evidence that the
385 polymerization is reversible and sensitive to amino acids, perhaps reflecting an allosteric sensing
386 mechanism. Additional cues affecting Glt1 polymerization may include potential changes in the
387 intracellular pH [55,67].
388
389 We provide evidence that the Glt1 assemblies fulfill the criteria of being *bona fide* aging factors:
390 1. They form in response to aging, 2. They are asymmetrically segregated between aged mother
391 cells and rejuvenating daughter cells, and 3. Preventing their formation extends life span [15,39]. Our
392 data show that Glt1 polymerization is associated with accumulation of amino acids suggesting that
393 at least two separate pathways contribute to age-associated amino acid overflow: defective
394 vacuolar compartmentalization [22,61] and Glt1 polymerization-mediated amino acid uptake and
395 glutamine transamination. We found that amino acid accumulation is linked to mitochondrial
396 dysfunction, potentially affecting the TCA cycle and mitochondrial iron-sulfur cluster proteins
397 [61,63]. Why then has polymerization been selected by evolution? In the wild, yeast cells do not grow
398 in test tubes but in colonies formed by interactive communities where cells may engage in cross-
399 generational amino acid exchange between young and aged cells [68]. Thus, Glt1 polymerization
400 could be an example of antagonistic pleiotropy that has evolved for the benefit of the community,
401 but at the cost of aging of the individual cell.
402
403 In addition to affecting the mitochondria, we propose that age-related amino acid accumulation
404 can lead to structural-functional alterations in proteins interacting with amino acids. For instance,
405 67 % of cytosolic aminoacyl-tRNA synthetases displayed structural changes during aging. This
406 might reflect altered binding status to cognate amino acids, potentially affecting tRNA charging
407 and fidelity of protein translation. Indeed, translation fidelity is important for life span regulation
408 in eukaryotes [31] in part by overwhelming the proteostasis machinery [32,51]. Our data support such a
409 chain of events. We provide evidence that ribosome-associated Hsp70 chaperones involved in
410 folding of nascent polypeptide chains are increasingly occupied by client interactions during aging.
411 Similar changes were found in the ER Hsp70 Kar2/BiP and cytosolic Hsp70 Ssa1, likely reflecting
412 increased occupancy of these chaperones by client proteins and their compartmentalization to
413 aging cells [25,47,69]. Such chaperone sequestering may lead to proteostasis collapse during later
414 stages of aging [47,70].

bioRxiv preprint doi: https://doi.org/10.1101/2023.01.23.524173; this version posted January 23, 2023. The copyright holder for this preprint (which was not certified by peer review) is the author/funder. All rights reserved. No reuse allowed without permission.

415 Taken together, understanding the landscape of protein structural changes during aging provides
416 opportunities to build novel hypotheses on how age-associated cellular changes at the pathway
417 level with mechanistic precision.

418

419 **Limitations of the study**

420 Our approach has some limitations that constrain the conclusions of our study. Our samples
421 comparing two timepoints in aging limit the conclusions to early aging processes. Even though
422 this is arguably the most informative way for capturing primary changes associated with aging, it
423 will be important in the future to construct a more comprehensive temporal map of aging-
424 associated protein structural changes. Although our data exposed known and novel processes
425 related to aging, some of the detected changes can also derive from differences between the mother
426 and daughter cells that are not related to aging *per se* [71]. The proteome coverage in our LiP-MS
427 analysis was 62.7 % of the expressed yeast proteome [72], so our study excludes a portion of the
428 proteome, primarily consisting of low abundant proteins. Furthermore, owing partially to the
429 limited resolution of the LiP-MS method, interpreting the nature of the structural change can be
430 challenging, as they can be associated with various causes, for example altered interactions,
431 folding or assembly change. Therefore, combining structural proteomics with secondary imaging-
432 based approaches [73] could be a powerful approach, as shown also in this study for a limited set of
433 proteins (Fig. S3). Finally, one intriguing challenge in the future is to gain a more comprehensive
434 understanding of how Glt1 polymerization is regulated and how it inflicts transcriptomic and
435 metabolic changes in aged cells.

bioRxiv preprint doi: https://doi.org/10.1101/2023.01.23.524173; this version posted January 23, 2023. The copyright holder for this preprint (which was not certified by peer review) is the author/funder. All rights reserved. No reuse allowed without permission.

436 **Main figure legends**
437
438 **Figure 1. Identification of age-related structural changes in pleiotropic regulators of cell**
439 **metabolism, growth, and stress responses**
440 **A.** Overview of workflow to identify age-related protein structural changes using LiP-MS.
441 **B.** Number of GO functions in age-altered proteins (light blue) compared to unaltered proteins
442 (grey).
443 **C.** Number of protein-protein interactions in age-altered proteins (n = 460) (light blue) compared
444 to unaltered proteins (n = 2279) (grey). Black line in box plots in (B-C) is median and whiskers
445 mark 10 and 90 percentile values.
446 **D.** Gene ontology (GO) enrichment by over-representation analysis of age-altered proteins
447 compared to unaltered proteins. The size of dots in the plot represents the number of proteins for
448 every biological process. The color change from blue to red signify the size of adjusted P value (P
449 adjusted < 0.05).
450 **E.** Fraction of aggregating proteins and superaggregators among age-altered proteins (n = 468)
451 (light blue) and unaltered proteins (n = 2332) (grey).
452 **F.** Fraction of stress granules forming proteins among age-altered proteins (n = 468) (light blue)
453 compared to unaltered proteins (n = 2332) (grey).
454 **G.** Fraction of asymmetrically retained long-lived proteins (LARPs) among age-altered proteins
455 (n = 468) (light blue) compared to unaltered proteins (n = 2332) (grey).
456 **H.** Fraction of genes whose decreased expression extends lifespan in age-altered (n = 468) (light
457 blue) and unaltered proteins (n = 2332) (grey) or their homologs in *S. cerevisiae* and *C. elegans*.
458 Statistical significance was assessed with Fisher´s exact test and effect size in (B-C) is displayed
459 as common language effect size (CLES) and in (E-H) as odds ratio (OR). **P < 0.01; ****P <
460 0.0001.
461
462 **Figure 2: Structural alterations indicate age-related protein activity changes in regulators of**
463 **proteostasis**
464 **A.** Cartoon representation of ADP-bound 'open' Hsp70 with the nucleotide binding domain in gray
465 and the substrate binding domain (SBD) in light green (PDB:2KHO; [74]). Close-up of the SBD with
466 Ssa1 LiP-peptides mapped in red and the peptide substrate in yellow (PDB:1DKX; [49]).
467 **B.** The chord plot depicts contacts between LiP peptide (red) and client peptide (orange) based on
468 (PDB:1DKX). The inner arcs display the contacting secondary structures.
469 **C**. Representative images of young and aged cells expressing Ssa1 tagged with GFP show
470 association of Ssa1 with protein aggregates in aged cells (arrowhead). Cell age can be determined
471 from bud scars on cell wall stained with calcofluor (magenta). Scale bar 2 µm.
472 **D.** Cartoon structure of *Pyrococcus horikoshii* Trm1. LiP-peptide depicted in red and AdoMet in
473 yellow. Close up showing two AdoMet interacting residues Asp78 and Ile79. (PDB: 2EJT; [52]).
474 **E.** Chord plot displays contacts between LiP peptide-region (red) and AdoMet (yellow). The inner
475 arcs depict contacting secondary structures.
476 **F.** Levels of N2,N2-dimethylguanosine ($m^{2,2}G$) modified tRNA increase in aged (mean age 4.4
477 divisions) cells compared to young (mean age 0.1 divisions) cells. TRNA levels were identified
478 by mass spectrometry and normalized to an internal ^{15}N-guanosine standard. Significance was
479 determined with two tailed unpaired t-test with Welch´s correction. n = 2. **P < 0.01.
480
481 **Figure 3: Glutamate synthase Glt1 forms filamentous polymers during aging**
482 **A.** Endogenous Glt1 tagged with GFP is soluble in young cells but forms a fiber-like polymers in
483 aged cells. Scale bar 1 µm.

bioRxiv preprint doi: https://doi.org/10.1101/2023.01.23.524173; this version posted January 23, 2023. The copyright holder for this preprint (which was not certified by peer review) is the author/funder. All rights reserved. No reuse allowed without permission.

484 **B.** Quantification of cells bearing Glt1 polymers between young (0-1 divisions, $n = 681$) and aged
485 (4-6 divisions, $n = 82$) cells.
486 **C.** Quantification of inheritance of Glt1 polymers by mother or daughter cells during cell division
487 by live-cell imaging. $n = 364$.
488 **D.** Quantification of cells with Glt1 polymers in varying amino acid conditions: no amino acids
489 (no AA), with peptone (no AA + peptone) and synthetic complete media (SC). $n = 3$.
490 **E.** representative time-lapse images from microfluidics-coupled microscopy analysis of Glt1-GFP
491 (green) polymer over time after switching to amino acid deprived media. Scale bar 1 µm.
492 **F.** Quantification of Glt1 polymer dynamics over time after switching to media without amino
493 acids. $n = 40$.
494 **G.** Correlative light-electron microscopy image of Glt1-GFP (green) polymer bearing cell detected
495 with fluorescence microscopy and subsequently visualized by transmission electron microscopy
496 (TEM). Area of Glt1 polymer denoted with the box. Scale bar is 1 µm and in the zoom-in EM
497 image (right) 200 nm.
498 **H.** Mating cells carrying Glt1 polymers tagged with mKate2 (red) or GFP (green). Time lapse
499 images of a stable co-assembly of two polymers. Scale bar 2 µm.
500 **I.** Time-lapse microscopic evaluation of Glt1-GFP polymer assembly. Scale bar 1 µm.
501 **J.** Dynamics of Glt1 polymer assembly was assessed by measuring the length of assemblies in
502 individual cells over 345 min after nucleation and plotted with two-phase association model,
503 showing duplication time for fast 7,943 min ($HalfLife_{FAST}$) and slow 175.6 min ($HalfLife_{slow}$)
504 states. Red line displaying model fit ($R^2 = 0.53$). $n = 77$.
505 **K.** Table summarizing identified LiP peptides in Glt1 and visualized in a structural model of yeast
506 Glt1 hexamer (PDB: 2VDC; [57]).
507 **L.** Color-coded representation of mutated residues in a Glt1 structural model. Table summarizes
508 the effect of the different mutants on Glt1 polymerization.
509 **M.** Representative images wild type and Glt1 H1537A, Y1538N, L1539S mutant cells tagged with
510 GFP. Scale bar 1 µm.
511 **N.** Cartoon model of putative polymerization mechanism of Glt1 with dihedral symmetry (D3).
512 Error bars in the graphs represent ± SD. Statistical significance was assessed with two tailed
513 unpaired t test (B-C) or one-way ANOVA with Dunnett´s correction. *$P < 0.05$; **$P < 0.01$, ****P
514 < 0.0001.
515

516 **Figure 4: Glt1 polymerization is reversible and promotes accumulation of intracellular**
517 **amino acids**
518 **A.** Replicative life span comparison between WT and *GLT1-MUT* cells. The median life span is
519 displayed on the graph. $n_{wt} = 40$, $n_{GLT1\text{-}MUT} = 62$. Statistical significance was assessed with Mantel-
520 Cox test.
521 **B.** Workflow for comparing transcriptomics and metabolomics. Purified fractions of young and
522 aged cells were subjected to RNAseq and steady-state metabolomics analysis or grown with
523 labelled $^{13}C_5{}^{15}N_2$-glutamine for tracing analysis.
524 **C.** Principal component analysis (PCA) of steady-state metabolomics. Young cell clusters
525 encircled with dotted lines, aged cell clusters with solid lines. $n = 4$.
526 **D.** Differences in steady-state metabolites between WT and *GLT1-MUT* are summarized in
527 orthogonal partial least square (OPLS) analysis. $n = 4$.
528 **E.** Feature importance graph of OPLS indicating metabolites and their weight with VIP score
529 between aged WT and *GLT1-MUT* (yellow higher and turquoise lower metabolites levels between
530 two groups). $n = 4$.
531 **F.** Fold change in steady-state amino acid levels with age in WT and *GLT1-MUT* cells $n = 4$.

bioRxiv preprint doi: https://doi.org/10.1101/2023.01.23.524173; this version posted January 23, 2023. The copyright holder for this preprint (which was not certified by peer review) is the author/funder. All rights reserved. No reuse allowed without permission.

532 **G.** Reaction catalyzed by Glt1.
533 **H.** The fractional contribution of labelled glutamate from Glt1 reaction. $n = 4$.
534 **I.** Fractional contribution of labelled $^{13}C_5$-$^{15}N_2$-glutamine uptake. $n = 4$.
535 **J.** Utilization of labelled $^{13}C_5$-$^{15}N_2$-glutamine for phenylalanine (Phe) synthesis via transamination
536 is shown by a ratio of labelled $^{13}C_5$-$^{15}N_2$-glutamine to ^{15}N-labelled Phe. $n = 4$.
537 **K.** Utilization of labelled $^{13}C_5$-$^{15}N_2$-glutamine for isoleucine/leucine (Ile/Leu) synthesis via
538 transamination shown by a ratio of labelled $^{13}C_5$-$^{15}N_2$-glutamine to ^{15}N-labelled Ile/Leu. $n = 4$.
539 **L.** Age-dependent analysis of mitochondrial membrane potential between WT and *GLT1-MUT*
540 cells. Correlation coefficient (R) and its significance was computed with standard Pearson´s
541 correlation test where the dots represent single cells and line indicates the linear regression curve.
542 $n_{WT} = 216$, $n_{GLT1\text{-}MUT} = 154$.
543 **M.** Quantification of MitoLoc signal in normal and high amino acid conditions in WT and *GLT1-*
544 *MUT* cells. $n_{WT} = 186$, $n_{GLT1\text{-}MUT} = 149$, at least 25 cells per subgroup was analyzed from 3
545 biological replicates. Error bars represent mean ± SD. Statistical significance in (H-K) was
546 assessed with ordinary one-way ANOVA with Dunnett´s correction and in M with three-way
547 ANOVA with Šidák´s correction. $^{*}P < 0.05$; $^{**}P < 0.01$; $^{**}P < 0.001$ $^{****}P < 0.0001$; n.s. not
548 significant.

bioRxiv preprint doi: https://doi.org/10.1101/2023.01.23.524173; this version posted January 23, 2023. The copyright holder for this preprint (which was not certified by peer review) is the author/funder. All rights reserved. No reuse allowed without permission.

549 **Key resources table**

REAGENT or RESOURCE	**SOURCE**	**IDENTIFIER**
Antibodies		
mouse 6x-His Tag Monoclonal Antibody (HIS.H8)	Thermo Fisher Scientific	MA1-21315 RRID:AB_2536988
mouse Anti-β-actin [8F10-G10]	Abcam	ab1700325 RRID:AB_2893492
rabbit Anti-PGK1 polyclonal antibody	Thermo Fisher Scientific	PA5-28612 RRID:AB_2546088
mouse Anti-GFP monoclonal antibody	Merck	11 814 460 001 RRID:AB_390913
Rabbit Anti-Mouse HRP	Invitrogen	A16166 RRID:AB_2534837
Goat anti-Rabbit HRP	Invitrogen	A27036 RRID:AB_2536099
Bacterial and virus strains		
Escherichia coli DH5α	Zymo Research	Mix & Go, CAT #T3007
Chemicals, peptides and recombinant proteins		
DnpI	Thermo Fisher Scientific	Cat #ER1701
EZ-link™ Sulfo-NHS-LC-Biotin	Thermo Fisher Scientific	Cat #21335
Streptavidin MicroBeads	Miltenyi Biotec	Cat #130-048-101
Fluorescent brightener 28 (Calcofluor)	Sigma-Aldrich	Cat # F3543
Concanavalin A	Sigma-Aldrich	Cat # C2010
carbonyl cyanide 3-chlorophenylhydrazone CCCP	Sigma-Aldrich	Cat #C2759
$^{13}C_5{}^{15}N_2$-Gln (CNLM-1275-PK)	Cambridge isotope laboratories	CNLM-1275-H-PK
100 mg/ml salmon sperm DNA	Sigma-Aldrich	Cat #D7656
Zymolyase 20T	Amsbio	Cat #120491-1
Concanamycin A	Santa Cruz Biotechnology	sc-202111
2′,7′-Bis(2-carboxyethyl)-5(6)-carboxyfluorescein acetoxymethyl ester (BCECF/AM)	Sigma-Aldrich	B8806
Monensin Sodium salt	Sigma-Aldrich	M5273
Nigericin Sodium salt	Sigma-Aldrich	SML-1779
Steptavidin, Alexa Fluor™ 633 conjugate	Thermo Fisher Scientific	Cat #S21375
Critical commercial assays		
Easy Clone 2.0 Yeast ToolKit	Addgene	Kit #1000000073
Pierce™ BCA Protein Assay Kit	Thermo Fisher Scientific	Cat #23225

bioRxiv preprint doi: https://doi.org/10.1101/2023.01.23.524173; this version posted January 23, 2023. The copyright holder for this preprint (which was not certified by peer review) is the author/funder. All rights reserved. No reuse allowed without permission.

Direct-zol RNA Miniprep Kit	Zymo Research	Cat #R2051
Experimental models: Organisms/strains		
WT BY4741: MATa his3Δ1 leu2Δ0 met15Δ0 ura3Δ0	[75]	
WT Mother Enrichement Program (MEP) MATa ade2::hisG his3 leu2 lys2 ura3D0 trp1D63 hoD::SCW11pr-Cre-EBD78-NatMX loxP-UBC9-loxP-LEU2 loxP-CDC20-Intron-loxP-HPHMX	[76]	
BY4741: MATa his3Δ1 leu2Δ0 met15Δ0 ura3Δ0 ASN1-GFP:HIS3	[77]	
BY4741: MATa his3Δ1 leu2Δ0 met15Δ0 ura3Δ0 ASN2-GFP:HIS3	[77]	
BY4741: MATa his3Δ1 leu2Δ0 met15Δ0 ura3Δ0 BAT2-GFP:HygMX	This study	
BY4741: MATa his3Δ1 leu2Δ0 met15Δ0 ura3Δ0 CAR1-GFP: HygMX	This study	
BY4741: MATa his3Δ1 leu2Δ0 met15Δ0 ura3Δ0 CAR2-GFP: HygMX	This study	
BY4741: MATa his3Δ1 leu2Δ0 met15Δ0 ura3Δ0 CYS3-GFP: HygMX	This study	
BY4741: MATa his3Δ1 leu2Δ0 met15Δ0 ura3Δ0 CYS4-GFP: HygMX	This study	
BY4741: MATa his3Δ1 leu2Δ0 met15Δ0 ura3Δ0 GDH1-GFP: HygMX	This study	
BY4741: MATa his3Δ1 leu2Δ0 met15Δ0 ura3Δ0 GDH2-GFP:HIS3	[77]	
BY4741: MATα his3Δ1 leu2Δ0 met15Δ0 ura3Δ0 GLT1-GFP:HIS3	[77]	
BY4741: MATa his3Δ1 leu2Δ0 met15Δ0 ura3Δ0 GLY1-GFP: HygMX	This study	
BY4741: MATa his3Δ1 leu2Δ0 met15Δ0 ura3Δ0 HOM2-GFP: HygMX	This study	
BY4741: MATa his3Δ1 leu2Δ0 met15Δ0 ura3Δ0 HOM6-GFP: HygMX	This study	
BY4741: MATa his3Δ1 leu2Δ0 met15Δ0 ura3Δ0 ILV6-GFP: HygMX	This study	
BY4741: MATa his3Δ1 leu2Δ0 met15Δ0 ura3Δ0 LYS1-GFP: HygMX	This study	
BY4741: MATa his3Δ1 leu2Δ0 met15Δ0 ura3Δ0 MET6-GFP:HIS3	[77]	
BY4741: MATa his3Δ1 leu2Δ0 met15Δ0 ura3Δ0 SER1-GFP: HygMX	This study	
BY4741: MATa his3Δ1 leu2Δ0 met15Δ0 ura3Δ0 SHM2 -GFP: HygMX	This study	

bioRxiv preprint doi: https://doi.org/10.1101/2023.01.23.524173; this version posted January 23, 2023. The copyright holder for this preprint (which was not certified by peer review) is the author/funder. All rights reserved. No reuse allowed without permission.

BY4741: MATa his3Δ1 leu2Δ0 met15Δ0 ura3Δ0 THR1-GFP: HIS3	[77]	
BY4741: MATa his3Δ1 leu2Δ0 met15Δ0 ura3Δ0 THR4-GFP: HygMX	This study	
BY4741: MATa his3Δ1 leu2Δ0 met15Δ0 ura3Δ0 TRP5-GFP: HygMX	This study	
BY4741: MATα his3Δ1 leu2Δ0 met15Δ0 ura3Δ0 GLT1-GFP: HIS3 HSP104-mCherry: KanMX	This study	
BY4741: MATα his3Δ1 leu2Δ0 met15Δ0 ura3Δ0 GLT1-mKate2:HygMX	This study	
BY4741: MATa his3Δ1 leu2Δ0 met15Δ0 ura3Δ0 GLT1H1537A,Y1538N,L1539S	This study	
BY4741: MATa his3Δ1 leu2Δ0 met15Δ0 ura3Δ0 GLT1H1537A,Y1538N,L1539S-GFP: HygMX	This study	
BY4741: MATa his3Δ1 leu2Δ0 met15Δ0 ura3Δ0 GLT1-GFP: HygMX	This study	
BY4741: MATa his3Δ1 leu2Δ0 met15Δ0 ura3Δ0 GLT1V1498T,L1500S,L1503S-GFP: HygMX	This study	
BY4741: MATa his3Δ1 leu2Δ0 met15Δ0 ura3Δ0 GLT1F1511N,V1512T,L1515S,I1516N-GFP: HygMX	This study	
BY4741: MATa his3Δ1 leu2Δ0 met15Δ0 ura3Δ0 GLT1V1553T,L1554S,L1555S-GFP: HygMX	This study	
BY4741: MATa his3Δ1 leu2Δ0 met15Δ0 ura3Δ0 Δgdh1:: KanMX	EUROSCARF deletion collection [78]	
BY4741: MATa his3Δ1 leu2Δ0 met15Δ0 ura3Δ0 Δgdh3:: KanMX	EUROSCARF deletion collection [78]	
BY4741: MATα his3Δ1 leu2Δ0 met15Δ0 ura3Δ0 Δgdh1:: KanMX Δgdh3:: KanMX	This study	
BY4741: MATα his3Δ1 leu2Δ0 met15Δ0 ura3Δ0 Δgdh1:: KanMX Δgdh3:: KanMX GLT1H1537A,Y1538N,L1539S	This study	
BY4741: MATα his3Δ1 leu2Δ0 met15Δ0 ura3Δ0 Δgdh1:: KanMX Δgdh3:: KanMX Δglt1::natNT2	This study	
BY4741: MATa his3Δ1 leu2Δ0 met15Δ0 ura3Δ0 DIP5-GFP: HygMX	This study	
BY4741: MATa his3Δ1 leu2Δ0 met15Δ0 ura3Δ0 GNP1-GFP: HygMX	This study	
BY4741: MATa his3Δ1 leu2Δ0 met15Δ0 ura3Δ0 GAP1-GFP: HygMX	This study	
BY4741: MATa his3Δ1 leu2Δ0 met15Δ0 ura3Δ0 GLT1H1537A,Y1538N,L1539S DIP5-GFP: HygMX	This study	

bioRxiv preprint doi: https://doi.org/10.1101/2023.01.23.524173; this version posted January 23, 2023. The copyright holder for this preprint (which was not certified by peer review) is the author/funder. All rights reserved. No reuse allowed without permission.

BY4741: MATa his3Δ1 leu2Δ0 met15Δ0 ura3Δ0 GLT1H1537A,Y1538N,L1539S GNP1-GFP: HygMX	This study	
BY4741: MATa his3Δ1 leu2Δ0 met15Δ0 ura3Δ0 GLT1H1537A,Y1538N,L1539S GAP1-GFP: HygMX	This study	
BY4741: MATa his3Δ1 leu2Δ0 met15Δ0 ura3Δ0, chrI::TERM$_{CYC1}$-preSU9-yeGFP-P$_{MET17}$::P$_{ADH1}$-preCOX4-mCherry::URA3	This study	
BY4741: MATa his3Δ1 leu2Δ0 met15Δ0 ura3Δ0 GLT1H1537A,Y1538N,L1539S, chrI::TERM$_{CYC1}$-preSU9-yeGFP-P$_{MET17}$::P$_{ADH1}$-preCOX4-mCherry::URA3	This study	
MEP MATa ade2::hisG his3 leu2 met15D::ADE2 ura3D0 trp1D63 hoD::SCW11pr-Cre-EBD78-NatMX loxP-UBC9-loxP-LEU2 loxP-CDC20-Intron-loxP-HPHMX SSA1-GFP:HIS3	[25]	
Recombinant DNA		
Plasmid: pYM44 (yeGFP-HIS3MX6)	[79] Euroscarf	P30256
Plasmid: pYM25 (yeGFP - hphNT1)	[79] Euroscarf	
Plasmid: pYM25-mK2 (mKate2 - hphNT1)	This study	
Plasmid: pYM25- GLT1- yeGFP - hphNT1	This study	
Plasmid: pYM25- GLT1V1498T,L1500S,L1503S-yeGFP - hphNT1	This study	
Plasmid: pYM25-GLT1F1511N,V1512T,L1515S,I1516N - yeGFP - hphNT1	This study	
Plasmid: pYM25- GLT1H1537A,Y1538N,L1539S - yeGFP - hphNT1	This study	
Plasmid: pYM25- GLT1V1553T,L1554S,L1555S - yeGFP - hphNT1	This study	
Plasmid: GAN230-TetR-mKate2	[80]	
Plasmid: pML104 CAS9 – URA3	[81]	
Plasmid: pML104 gRNA_GLT1 4608_CAS9 – URA3	This study	
Plasmid: pMitoLoc TERM$_{CYC1}$-preSU9-yeGFP-P$_{MET17}$ - P$_{ADH1}$-preCOX4-mCherry - natMX6		
Plasmid: CfB2188	Easy Clone 2.0 (Addgene)	RRID:Addgene_39296
Plasmid: pFA6a-kanMX6	[79] Euroscarf	39296
Plasmid: pFA6-natNT2	[79] Euroscarf	P30346
Software and algorithms		
gRNA design tool for CRISPR	http://wyrickbioinfo2.smb.wsu.edu/crispr.html	

bioRxiv preprint doi: https://doi.org/10.1101/2023.01.23.524173; this version posted January 23, 2023. The copyright holder for this preprint (which was not certified by peer review) is the author/funder. All rights reserved. No reuse allowed without permission.

FIJI ImageJ: MitoLoc and Yeast correlation plug in	64 64	
GraphPad Prism version 9	Dotmatics	
MetaboAnalyst version 5	https://www.metaboanalyst.ca/	
R v4.1.0	Vigorous Calisthenics	
FlowJo v10	BD Biosciences	

550

551 **Experimental model and subject details**

552 Yeast strains and plasmids

553 All strains used in this study are derivatives of *Saccharomyces cerevisiae* S288c (BY4741) [75] and
554 are listed in resource table. Endogenous gene tagging with GFP, mCherry or mKate2 were done
555 by homologous recombination[79]. Briefly, primers annealing to the tagging cassette in the plasmid
556 with additional 45 – 55 bp overhangs homologous to a place upstream and downstream of the
557 STOP codon of desired gene were constructed. Tagging plasmid with mKate2 fluorophore YM25-
558 mK2 was constructed by replacing GFP from YM25 plasmid[79] with mKate2 from GAN230-TetR-
559 mKate2 [80] plasmid by homologous recombination in *Escherichia coli* DH5α cells [82]. For this,
560 YM25 was linearized to exclude GFP by PCR and mKate2 was amplified from the plasmid
561 GAN230-TetR-mKate2 with primers containing 25 bp overhangs complementary to linearized
562 YM25. Purified fragments were assembled by mixing them vector:insert ratio of 1:3 and
563 transforming them into *E. coli* DH5α strain [82] [82]. For genomic integration of MitoLoc, EasyClone
564 2.0 (Addgene) was used. Functional elements of original pMitoLoc $TERM_{CYC1}$-preSU9-yeGFP-
565 P_{MET17} - P_{ADH1}-preCOX4-mCherry - natMX6 [64] was amplified with P1_f and G1_r primers and
566 inserted in pCfB2188 plasmid. For genomic integrations into chromosome X, plasmid was cut
567 with NotI and transformed into yeast (see Yeast transformation).

568

569 For Glt1 mutagenesis, GLT1 gene was inserted into GFP tagging plasmid YM25. First YM25
570 plasmid was linearized with PCR and assembled with GLT1 PCR fragment that contains 35 bp
571 overhangs complementary to the plasmid by homologous recombination in *E. coli* DH5α strain [82].
572 For this, purified PCR fragments were mixed with vector:insert ratio 1:3 and transformed to *E.*
573 *coli* DH5α strain. Then primers with certain mismatches in GLT1 gene were designed so that the
574 round-the-clock amplified YM25-GLT1-GFP plasmid would contain desired mutations. Reaction
575 mixtures were treated with restriction enzyme DnpI (Thermo Fischer Scientific) to disrupt
576 template DNA and transformed into *E. coli* DH5α strain. Newly generated plasmids were
577 sequenced and inserted into yeast cells by homologous recombination with primers homologous
578 to the sequence upstream and downstream of the gene (S1 and S2) to replace genomic GLT1 with
579 GFP-tagged mutants (Janke *et al.*, 2004).

580

581 Endogenous non-polymerizing GLT1 mutant H1537A, Y1538N, L1539S without tags or selection
582 markers were generated with CRISPR-Cas9 system in yeast [81] and were used in experiments Fig.
583 4 and 5 and associated supplementary figures. Primers for gRNA were created with the online tool
584 (http://wyrickbioinfo2.smb.wsu.edu/crispr.html) and the primer which was closest to the target
585 sequence was selected at the position 4608 bp in the open reading frame. Vector for Glt1 mutation

bioRxiv preprint doi: https://doi.org/10.1101/2023.01.23.524173; this version posted January 23, 2023. The copyright holder for this preprint (which was not certified by peer review) is the author/funder. All rights reserved. No reuse allowed without permission.

586 by CRISPR-Cas9 was prepared by ligating annealed and phosphorylated gRNA oligonucleotides
587 with Smi/BclI digested plasmid pML104 [81]. After sequencing, newly generated plasmid together
588 with annealed 100 bp repair template containing desired mutation were transformed into yeast.
589 Correct mutagenesis was confirmed with sequencing and Cas9 expressing plasmid was eliminated
590 by streaking correct clone on YPD plate and selecting for single colonies which were no longer
591 able to grow in absence of uracil.
592
593 Yeast cell culture, media and drug treatments
594 Cells were grown in exponential phase in YPD medium (1 % yeast extract, 2% Bacto peptone, 2%
595 glucose) for 24 h before every experiment. Media were exchanged by washing cells twice with
596 PBS and resuspending in the medium of interest. Media types refer to medium without amino acids
597 (no AA) (6,7g/L YNB base, 2% glucose), minimal medium (MM) (0,02 g/L of Ura, Met, Leu, His,
598 6.7 g/L YNB base, 2% glucose), Synthetic minimal medium (SD) (0,02 g/L L-Ade, L-Arg, L-His,
599 L-Met, L-Trp, Ura, 0.03 g/L L-Ile, L-Lys, L-Tyr, 0.05 g/L L-Phe, 0.1 g/L L-Leu, 0.15 g/L L-Val,
600 0.2 g/L L-Thr, 6.7g/L YNB base, 2% glucose), Synthetic complete medium (SC) (0.013 g/L L-
601 Ade, 0.35 g/L L-Arg, L-inositol, 0.26 g/L L-Asp, L-Leu, 0.,057 g/L L-His, 0.52 g/L L-Ile, 0.09
602 g/L L-Lys, 0.19 g/L L-Met, 0.082 g/L L-Phe, L-Trp, 0.01 g/L L-Ser, 0.12 g/L L-Thr, L-Val, 0.013
603 g/L L-Ade, 0.018 g/L L-Tyr, 0.013 g/L L-Ade, 0.02 g/L Ura, 6.7 g/L YNB base, 2% glucose).
604 Special additives were added to the final concentration of 2% Bacto peptone, 10 μM carbonyl
605 cyanide 3-chlorophenylhydrazone (CCCP), 500 nM concanamycin A (ConcA).
606
607 **Methods details**
608 Transformation of yeast
609 Overnight yeast cell culture was diluted to OD_{600} 0.1 in liquid YPD media and grown until it
610 reached OD_{600} 0.6. Then cells were pelleted by centrifuging them at 500 *g* for 5 min and washed
611 twice with transformation buffer (100 mM LiOAc, 10 mM Tris, 1 mM EDTA, pH 8). Then cell
612 pellet was resuspended in 72 µl transformation buffer and mixed with plasmid DNA (2 µl) or PCR
613 product (10µl), 8 µl of 100 mg/ml salmon sperm DNA (prior to use boiled for 10min at 100 °C
614 and cooled down on ice), 500 µl of PEG buffer (40% PEG-3350 (m/V), 100 mM LiOAc, 10 mM
615 Tris, 1 mM EDTA, pH 8) and incubated in room temperature for 30 min. Then 65 µl of DMSO
616 was added and yeast were subjected to heat shock at 42 °C for 15 min and spun down at 300 *g* for
617 5 min. If no auxotrophic marker was used for selection, yeast pellets were resuspended into 100 µl
618 of corresponding media and plated on agar plates with the same media. If antibiotics were used,
619 samples were incubated in 3 ml of YPD media for 2 – 3 h and then plated on YPD plates with
620 antibiotics.
621
622 Purification of young and aged yeast cells by magnetic-activated cell sorting
623 For young cell (0-1 generations) purification, cells were grown in exponential phase in YPD media
624 for 24 h before biotinylation. Then 2 x 10^8 cells were washed three times with PBS, resuspended
625 in 3 mg/ml Sulfo-NHS-LC-Biotin (Thermo Fischer Scientific) solution in PBS and incubated on
626 a rocking platform in room temperature for 30 min. Then cells were washed twice and resuspended
627 in 200 ml of prewarmed YPD media. After 2.5 h of growth in 130 rpm at 30 °C, cells were
628 harvested and resuspended into 2 x 10^8 cells/ml in PBS with 2 mM EDTA and 1:20 of the volume
629 of Streptavidin MicroBeads (Miltenyi Biotec). Cells were incubated on a rocking platform for 30
630 min in 4 °C and later resuspended into 12 ml of ice-cold PBS with 2 mM EDTA. Young cells were

bioRxiv preprint doi: https://doi.org/10.1101/2023.01.23.524173; this version posted January 23, 2023. The copyright holder for this preprint (which was not certified by peer review) is the author/funder. All rights reserved. No reuse allowed without permission.

631 collected by passing cell suspension through the MS column (Miltenyi Biotec) attached to a
632 magnetic stand and collecting flow through supernatant.
633 For aged cell (4-6 generations) purification, the procedure is the same, except that after
634 biotinylation cells are grown in 500 ml of prewarmed YPD media for 6 h. Then when cells are put
635 into the column, the column is washed 4 times with LiP buffer (20 mM hepes, 150 mM KCl, 10
636 mM $MgCl_2$) for LiP-MS analysis and in PBS for metabolomics and RNA-seq analyses. Aged cells
637 were eluted in LiP buffer or PBS by removing MS column from the magnetic stand.
638 After purification cells were resuspended into 1 ml of ice-cold LiP buffer or PBS and small amount
639 of cell suspension was taken to access cell number with cell counter. The required number of cells
640 was then divided into separate 1.5 ml tubes, spun down to remove supernatant and the pellet was
641 snap frozen with liquid nitrogen for storage or directly used for downstream applications. In
642 addition, a few microliters of initial purified cell culture were stained with calcofluor 10 µg/ml
643 (from 1 mg/ml stock in DMSO) and fixed by adding two volumes of cell suspension of 4% PFA
644 incubating cells for 15 min. In addition to calcofluor, streptavidin conjugated to Alexa Fluor™
645 633 was added to the fixation samples for only aged cells for assessing the purity of purification
646 by tracking initially biotinylated cells. After fixation, cells were centrifuged and the pellet was
647 resuspended into 4 µl Mowiol-DABCO mounting media and put on a glass slide with thin glass
648 cover slip. Cell age was assessed with microscopy (see Microscopy and live imaging) by
649 calculating bud scars in calcofluor stained cell wall for at least 100 cells for each sample.
650

651 Native protein extraction for LiP-MS
652 Cells were pelleted at 3000 *g* for 5 minutes at 4 °C and washed twice with ice-cold LiP-buffer (20
653 mM Hepes, 150 mM KCl, 10 mM $MgCl_2$, pH 7.5), and subsequently resuspended in 1 mL LiP-
654 buffer. Resuspended mixtures were snap-frozen in droplets by pipetting into liquid nitrogen. Lysis
655 of the snap-frozen cell suspension droplets was performed using a 6775 Freezer/Mill Instrument
656 (Thomas Scientific, Swedesboro, NJ, USA) according to the manufacturer's instructions. Protein
657 concentration of the resulted cell lysates (without clearing by centrifugation) were determined with
658 bicinchoninic acid assay (BCA Protein Assay Kit, Thermo Scientific, Rockford, IL).
659 Limited proteolysis (LiP) was performed as previously described[41]. Briefly, 100 µg of lysate was
660 subjected to Proteinase K (Sigma Aldrich) treatment at an enzyme to substrate ratio (E:S) of 1:100
661 at RT. The LiP reaction was stopped by boiling in a water bath at > 95 °C. Complete protein
662 denaturation was achieved by adding sodium deoxycholate (DOC) (Sigma Aldrich) to a final
663 concentration of 5% (w/v). Disulfide bridges were reduced by adding tris(2-
664 carboxyethyl)phosphine TCEP to a final concentration of 5 mM and incubation at 37 °C for 30
665 minutes. Reduced cysteine residues were alkylated by adding iodoacetamide IAA to a final
666 concentration of 40 mM and incubation of 45 minutes at RT in the dark. Tryptic peptides were
667 obtained by a first digestion with LysC (Wako Pure Chemical Industries) at an E:S of 1:100 for 4
668 h at 37 °C, followed by a second digestion with Trypsin (Promega) at an E:S of 1:100 overnight
669 at 37 °C. For the digestion steps, DOC concentration and pH were adjusted to the optimal values
670 as previously reported [41]. Digestion was stopped by adjusting the pH to < 3 and precipitated DOC
671 was removed by centrifugation. Finally, resulted peptides were desalted using Sep-Pak column
672 (Waters) according to manufacturer's instructions.
673 Peptides were separated using an online EASY-nLC 1000 HPLC system (Thermo Fisher
674 Scientific) operated with a 15 cm long in house packed reversed-phase analytical column (Reprosil
675 Pur C18 Aq, Dr. Maisch, 1.9 mm) before being measured on a Q-Exactive Plus (QE+) mass
676 spectrometer. A linear gradient from 5%–25% acetonitrile in 140 min at a flowrate of 300 nl/min
677 was used to elute the peptides from the column. Precursor ion scans were measured at a resolution
678 of 70,000 at 200 m/z and 20 MS/MS spectra were acquired after higher-energy collision induced

bioRxiv preprint doi: https://doi.org/10.1101/2023.01.23.524173; this version posted January 23, 2023. The copyright holder for this preprint (which was not certified by peer review) is the author/funder. All rights reserved. No reuse allowed without permission.

679 dissociation (HCD) in the Orbitrap at a resolution of 17,500 at 200 m/z per scan. The ion count
680 threshold was set at 1,00 to trigger MS/MS, with a dynamic exclusion of 25 s. Raw data were
681 searched against the S. cerevisiae Uniprot database using SEQUEST embedded in the Proteome
682 Discoverer software (both Thermo Fisher Scientific). Digestion enzyme was set to trypsin,
683 allowing up to two missed cleavages, one non-tryptic terminus and no cleavages at KP (lysine-
684 proline) and RP (arginine-proline) sites. Precursor and fragment mass tolerance was set at 10 ppm
685 and 0.02 Da, respectively. Carbamidomethylation of cysteines (+57.021 Da) was set as static
686 modification whereas oxidation (+15.995 Da) of methionine was set as dynamic modification.
687 False discovery rate (FDR) was estimated by the Percolator (embedded in Proteome Discoverer)
688 and the filtering threshold was set to 1%. Label-free quantitation was performed using the
689 Progenesis-QI Software (Nonlinear Dynamics, Waters). Raw data files were imported directly into
690 Progenesis for analysis. MS1 feature identification was achieved by importing the filtered search
691 results (as described above) from Proteome Discoverer into Progenesis to map the corresponding
692 peptides based on their m/z and retention times. Annotated peptides were then quantified using the
693 areas under their extracted ion chromatograms.
694
695 3D structural analyses
696 LiP conformotypic peptides were mapped to available protein structures to analyze the overlap of
697 these structural alterations and functionally relevant sites within the protein (e.g., substrate binding
698 sites). The EMBOSS Needle tool (EMBL-EBI) was used for pairwise sequence alignment of yeast
699 protein sequences with homologous proteins. Structural analyses and visualization were performed
700 with UCSF ChimeraX-1.1. [83,84]. *Escherichia coli* DnaK protein structures were used to visualize
701 conformotypic peptides of the yeast Hsp70 proteins (Ssa1, Ssb1, Ssb2 and Kar2) in open
702 conformation (Protein Data Bank (PDB) ID: PDB:4B9Q) [85], closed conformation (PDB:2KHO) [74]
703 and the substrate binding domain (SBD) in complex with a substrate peptide (PDB:1DKX) [49]. The
704 yeast Trm1 conformotypic peptide was mapped to a *Pyrococcus horikoshii* Trm1-S-adenosyl-L-
705 Methionine complex structure (PDB:2EJT) [52].
706 A model of the Glt1 structure was created by SWISS-MODEL homology modeling server [86] using
707 a homologous structure, glutamate synthases from *Azospirillum Brasilense* (PDB: 2VDC), as a
708 template [57]. Two types of Glt1 oligomers, with either C3 or D3 symmetry, were created by aligning
709 the homology model with the symmetry-related chains in the D3 symmetric complex of the
710 template structure using the Matchmaker tool in UCSF ChimeraX [84]. Figures of the oligomers
711 highlighting the peptides identified by LiP / MS and mutated residues were created in the same
712 software.
713
714 Contact site analysis
715 Chord plots illustrating contact sites between LiP peptide region in age-altered proteins and their
716 clients were created using information on non-covalent contacts from the Protein Contact Atlas or
717 custom data and processed with a python script to create a matrix of contacts between a protein
718 and a client peptide. If suitable data was not available in Protein Contact Atlas, the non-covalent
719 bonds were calculated with the coordinates provided in the PDB structure. Chord plots illustrations
720 on client peptide bound to Hsp70s were based on *E. coli* DnaK (PDB:1DKX) [49] and chord plots on
721 Trm1 bound to S-adenosyl-L-Methionine was based on Trm1 from *P. horikoshii* (PDB:2EJT) [52].
722 Distances between pairs of atoms were defined with Euclidean distance. The radii of the atoms in
723 contact were reduced from the distance. The radii of protein atoms were defined as previously
724 described [87] and for client peptide atoms, Van der Waals radii were used. The threshold for non-
725 covalent contact was set to 4 Å [50]. The matrixes were imported to R 4.1.0 and plots were created
726 with circlize package v0.4.15 chordDiagram function.

bioRxiv preprint doi: https://doi.org/10.1101/2023.01.23.524173; this version posted January 23, 2023. The copyright holder for this preprint (which was not certified by peer review) is the author/funder. All rights reserved. No reuse allowed without permission.

727
728 Microscopy and microfluidics
729 Before imaging experiments, cells were grown in exponential phase in YPD media for 24 h and
730 then were washed twice with PBS and resuspended in colorless media (for details see Yeast cell
731 culture and media). Cells in colorless media were grown on a spinning wheel for 4.5 – 6 h and
732 1.26 x 10^6 cells were stained with 100 µg/ml calcofluor for 5 min. Cells were washed once and
733 resuspended into 1 ml of media. A small amount 50 µl of cell suspension was added to a well in a
734 96 thin glass bottom imaging well-plate pre-coated with concanavalin A (Sigma Aldrich) and
735 topped up with 200 µl of colorless media. Well coating was performed by adding 100 µl of 2 mg/ml
736 concanavalin A solution in (PBS with 50 mM of $MnSO_4$ and 50 mM $CaCl_2$), incubating in room
737 temperature for 30 min and washing wells once with 150 µl of PBS.
738 Imaging was performed with customized Olympus IX-73 inverted widefield fluorescent
739 microscope DeltaVision Ultra (GE Healthcare) equipped with Pco edge 4.2ge sCMOS camera
740 CentOS 7 Linux operating system. Imaging was done using 60x or 100x oil objectives and,
741 depending on the fluorophore properties, with Blue (ex. 390 nm – em. 435 nm), Green (ex. 475
742 nm – em. 525 nm), Red (ex. 575 nm – em. 625 nm) and Far Red (ex. 632 nm – em. 679 nm) filter
743 settings.
744 Microfluidic experiments were performed with CellASIC® ONIX2 microfluidic operating system
745 with CellASIC® ONIX2 Y04C microfluidics plates, using manufacturer's instructions. The
746 imaging was performed with DeltaVision microscope as described above.
747
748 Correlative light and electron microscopy (CLEM)
749 Yeast expressing Glt1-GFP were grown overnight in exponential phase in SD liquid media before
750 the fixation. Then, 200 mL of the culture containing around 2.5 x 10^6 cells was added to a 1 mg/mL
751 Poly-L-Lysine (Sigma Aldrich) pre-coated MatTek dish with a gridded cover slip. The culture was
752 incubated for 10 min at room temperature to allow cell sedimentation before removing the SD
753 media and adding 200 mL of a fixative solution (3 % PFA, 0.5 % glutaraldehyde, 0.2 M citrate-
754 phosphate buffer, pH 5.5). After 1 h incubation, samples were washed three times with 0.2 M
755 citrate-phosphate buffer (pH 5.5) by keeping the washing solution on the sample dish for 5 min
756 and 2 ml of the same buffer was added to fixed cells. Then cells were imaged with widefield
757 fluorescent microscope DeltaVision Ultra (GE Healthcare) using brightfield channel and 60x oil
758 objective (see Microscopy and live imaging) and cells of interest were located on the MatTek grid.
759 Next, samples were fixed for electron microscopy by incubating the cells in fixative solution (2%
760 glutaraldehyde, 3% PFA, 0.2 M citrate-phosphate buffer, pH 5.5) for 30 min at room temperature.
761 After washing with 0.2 M citrate-phosphate buffer and distilled water, the cells were post-fixed
762 with 2% potassium permanganate for 1 h, on ice. Prior gradual infiltration into low viscosity epoxy
763 (TAAB, Aldermaston, UK) the samples were subjected to dehydration by increasing
764 concentrations of ethanol. After incubating 2 x 3 h with 100% epoxy, the block was polymerized
765 at 60°C for 16 h. The block was removed from the cover slip and a pyramid was trimmed according
766 to the finder grid pattern transferred to the block surface. Serial 60-nm-thick sections were cut with
767 an ultramicrotome (Leica EM Ultracut UC6i or UC7, Leica Mikrosysteme GmbH, Austria) and
768 collected on Pioloform coated, single slot grids. The sections were post-stained with uranyl acetate
769 and lead citrate and examined using a Hitachi HT7800 transmission electron microscope (Hitachi
770 High-Technologies, Tokyo, Japan) operated at 100 kV, and a Rio9 CMOS-camera (Gatan Inc.,
771 AMETEK, Pleasanton, CA).

bioRxiv preprint doi: https://doi.org/10.1101/2023.01.23.524173; this version posted January 23, 2023. The copyright holder for this preprint (which was not certified by peer review) is the author/funder. All rights reserved. No reuse allowed without permission.

772

773 tRNA isolation and $m^{2,2}G$ quantification by UPLC/MS

774 TRNA was isolated from young and aged cells (see Purification of young and aged yeast cells by
775 magnetic-activated cell sorting) as previously described [88] with the following modifications.
776 Briefly, approx. 10^8 of young or aged cells were resuspended in 250 µL of 0.9% NaCl and lysed
777 in an equal volume of acidic phenol (pH 4.3) with 1/5 volume of 1-bromo-3-chloropropane (BCP)
778 and glass beads. Cells were sheared by vortexing for 5 min at full speed, followed by centrifugation
779 for 15 min at 10 000 *g*, 22 °C. The aqueous phase was then transferred to a new centrifugation
780 tube and re-extracted with acidic phenol/BCP. The re-extracted aqueous phase was collected and
781 the volume was adjusted to 10 ml with equilibration buffer EQ (10 mM Tris-HCl pH 6.3, 15%
782 ethanol, 200 mM KCl), after which it was applied onto a pre-equilibrated (EQ buffer containing
783 0.15% Triton X-100) Nucleobond AX-100 column (Macherey-Nagel). The column was washed
784 twice with wash buffer WB (10 mM Tris-HCl pH 6.3, 15% ethanol, 300 mM KCl). TRNA was
785 eluted with 10 mL of elution buffer EB (10 mM Tris-HCl pH 6.3, 15% ethanol, 750 mM KCl) into
786 2.5 vol. of 99.6% ethanol. The tRNA was precipitated O/N at −20 °C and pelleted by centrifugation
787 for 30 min at 10 000 *g*, 4 °C. Residual salt was removed by washing the pellet with 80% ethanol.
788 Then, tRNA pellet was air-dried at RT and re-suspended in RNase/DNase-free water.
789 Dephosphorylated monoribonucleosides for MS analysis were generated as previously described
790 [89]. For data normalization, cleaved monoribonucleosides were spiked with ^{15}N-labeled
791 ribonucleosides, which served as an internal standard (25 ng ^{15}N-labelled ribonucleosides per 100
792 ng of sample). Samples were analyzed as described in [90] using a Waters Acquity® UPLC system
793 attached to a Waters Synapt G2 HDMS mass spectrometer via an ESI ion source.

794

795 Metabolite profiling

796 Before extraction young and old yeast cells were purified with magnetic sorter (see Purification of
797 young and aged yeast cells by magnetic-activated cell sorting). 2.5 x 10^7 cells were taken for steady
798 state metabolomics. For flux analysis 2.5 x 10^7 cells were treated in SC media with labeled 6.5
799 mM $^{13}C_5{}^{15}N_2$-Gln (CNLM-1275-PK) for 30 min pulse. The yeast suspension was washed twice
800 with 1xPBS, and metabolites were extracted with 500µl ice-cold buffer acetonitrile:ddH_2O
801 (80:20). Subsequently, the samples were sonicated 2 min and vortexed for 30 s for 3 rounds in
802 total, centrifuged 16 000 *g*, 10 min at +4°C and the supernatant was taken to further analysis.
803 All samples were analyzed on Thermo Q Exactive Focus Quadrupole Orbitrap mass spectrometer
804 coupled with a Thermo Dionex UltiMate 3000 HPLC system (Thermo Fisher Scientific, Inc.). The
805 HPLC was equipped with a hydrophilic ZIC-pHILIC column (150 × 2.1 mm, 5 µm) with a ZIC-
806 pHILIC guard column (20 × 2.1 mm, 5 µm, Merck Sequant). 5 µl of the samples were injected
807 into the LC-MS after quality controls in randomized order having every 10th sample as blank. The
808 separation was achieved by applying a linear solvent gradient in decreasing organic solvent (80–
809 35%, 16 min) at 0.15 ml/min flow rate and 45°C column oven temperature. The mobile phases
810 were following, aqueous 200 mmol/l ammonium bicarbonate solution (pH 9.3, adjusted with 25%
811 ammonium hydroxide), 100% acetonitrile and 100% water. The amount of the ammonium
812 bicarbonate solution was kept at 10% throughout the run resulting in steady 20 mmol/l
813 concentration. Metabolites were analyzed using a MS equipped with a heated electrospray
814 ionization (H-ESI) source using polarity switching and following setting: resolution of 70,000 at
815 *m/z* of 200, the spray voltages: 3400 V for positive and 3000 V for negative mode, the sheath gas:
816 28 arbitrary units (AU), and the auxiliary gas: 8AU, the temperature of the vaporizer: 280°C,
817 temperature of the ion transfer tube: 300 °C. Instrument control was conducted with the Xcalibur
818 4.1.31.9 software (Thermo Scientific). The peaks for metabolites were confirmed using
819 commercial standards (Merck Cambridge Isotope Laboratories & Santa Cruz Biotechnology). The

bioRxiv preprint doi: https://doi.org/10.1101/2023.01.23.524173; this version posted January 23, 2023. The copyright holder for this preprint (which was not certified by peer review) is the author/funder. All rights reserved. No reuse allowed without permission.

820 final peak integration was done with the TraceFinder 4.1 SP2 software (Thermo Scientific) and
821 for further data analysis, the peak area data was exported as excel file.
822

823 Transcriptomic profiling

824 After young and aged cell purification (see Purification of young and aged yeast cells by magnetic-
825 activated cell sorting), pellets containing 2.5 x 10^7 cells were resuspended with 800 µl of TRI
826 reagent (Zymo research) and placed in 2 ml Touch Micro-Organism Lysing Mix tubes (Omni). In
827 total, 4 replicates for each group were used. Then, cells were mechanically disrupted with Precellys
828 24 Tissue Homogenizer (Bertin Instruments) at 6000 rpm for 15s for a total of 4 cycles with 2 min
829 break on ice between cycles. RNA was further extracted using Direct-zol RNA Miniprep Kit
830 (Zymo Research) following manufacturer´s instructions. RNA concentration and purity was
831 measured by NanoDrop, and RNA samples were stored at -80 °C before use.
832 RNA-seq library preparation and sequencing were performed by the Sequencing Unit of Institute
833 of Molecular Medicine Finland FIMM Technology Centre at the University of Helsinki. Illumina
834 TruSeq Stranded mRNA library preparation Kit (Illumina) and NextSeq 500 Mid Output Kit PE75
835 (120 M reads) (Illumina) were used following manufacturer´s instructions.
836

837 Protein extraction and Western Blot

838 Cells were harvested by centrifugation and the pellet containing 6 – 8 x 10^7 cells was resuspended
839 in 250 µl Lysis Solution (0,25 M NaOH, 1% β-mercaptoethanol (v/v)) and 160 µl of 50%
840 Trichloroacetic acid. After 10 min incubation on ice, cells were centrifuged at high speed (21 500
841 *g*) for 3 min and the pellet was subjected to 1 ml acetone. Samples were centrifuged again and the
842 pellet was resuspended into sample buffer (120 mM Tris-HCl pH 6.8, 2% SDS) and heated in 95
843 °C for 5 min. Small amount of samples was used for quantification of protein concentration with
844 BCA Protein assay Kit (Thermo Fisher Scientific) and 6x loading buffer (48% glycerol and 0,03%
845 bromphenolblue) was added to the rest of the sample. For each sample 10 – 15 µg of protein was
846 loaded on a SDS-PAGE gel. For Glt1 detection via Western blot primary mouse Anti-GFP (Sigma-
847 Aldrich) or mouse Anti-6x-His Tag (HIS.H8) (Thermo Fisher Scientific) antibodies were used. As
848 a loading control primary rabbit Anti-PGK1 or mouse Anti-β-actin [8F10-G10] antibodies were
849 used. For detection horseradish peroxidase (HRP) conjugated Rabbit Anti-Mouse (Invitrogen) or
850 Goat anti-Rabbit (Invitrogen) secondary antibodies were used.
851

852 Flow cytometry

853 Cells were grown in exponential phase for 24 h before biotinylation to distinguish aged cell
854 fraction. For that, cells were washed three times with PBS and resuspended in 2 mg/ml Sulfo-
855 NHS-LC-Biotin (Thermo Fischer Scientific) solution in PBS and incubated on a rocking platform
856 in room temperature for 30 min. Then cells were washed twice and resuspended in colorless SD
857 media at the density of 5 x 10^4 cells/ml. Cells were grown in 30 °C for 10 h to facilitate aging of
858 biotinylated cells. Then, approx. 2 x 10^6 cells were taken and stained with Steptavidin-Alexa
859 Fluor™ 633 at the final concentration of 20 µg/ml for 5 min. Cells were washed with PBS and
860 resuspended in 1 ml of colorless SD media in a Falcon flowcytometry tube.
861 For vacuolar pH measurements, cells were incubated with 50 µM of 2′,7′-Bis(2-carboxyethyl)-
862 5(6)-carboxyfluorescein acetoxymethyl ester (BCECF/AM) for 30 min at 30 °C just before
863 staining with Steptavidin-Alexa Fluor™ 633. Calibration curve was made my resuspending
864 BCECF/AM stained cells in calibration buffer (50 mM MES, 50 mM HEPES, 50 mM KCl, 50
865 mM NaCl, 0.2 M ammonium acetate, 10 mM sodium azide, 110 uM monensin and 15 uM
866 nigericin) of different pH (5.5, 6.0, 6.5, 7.0, 7.5).

bioRxiv preprint doi: https://doi.org/10.1101/2023.01.23.524173; this version posted January 23, 2023. The copyright holder for this preprint (which was not certified by peer review) is the author/funder. All rights reserved. No reuse allowed without permission.

867 Cells were analyzed with BD LSRFortessa Flow Cytometer at the Flow Cytometry Unit in the
868 University of Helsinki. GFP fluorophore was exited with 488 nm laser and optical filter 530/30
869 (515-545 nm), BCECF/AM was excited with 405 nm laser optical filter 525/50 (500-550 nm) and
870 488 nm 530/30 (515-545 nm) and for Alexa Fluor™ 633 fluorophore 640 nm laser and 670/30
871 (655-685 nm) optical filter were used. Samples were collected by gating aged Steptavidin-Alexa
872 Fluor™ 633 positive cells and collecting 10 000 events per sample.
873 Flow cytometry data analysis was performed with FlowJo v10 software. Vacuolar pH of
874 BCECF/AM stained cells was determined from signal in 488 nm /405 nm ratio and interpolated
875 from the calibration curve using GraphPad v9 software.
876
877 Replicative life span assay
878 Single cells of wt and non-polymerizing Glt1 mutant (H1537A, Y1538N, L1539S) were placed on
879 YPD plate. After the first division, the daughters were selected for the aging experiment and the
880 mother cells were discarded. These selected cells were then followed through their replicative
881 lifespan by removing newly divided daughter cells. Cell replicative life span was followed for 12
882 h in 30 °C following by incubation in + 4 °C overnight. Finite number of divisions for each cell
883 were then plotted to generate the survival curves. The experiment was conducted with 3 biological
884 replicates, $N_{mutant} = 62$, $N_{wt} = 40$.
885
886 Oxygen consumption assay
887 After young and aged cell purification (see Purification of young and aged yeast cells by magnetic-
888 activated cell sorting) equal amount of $1.4 * 10^7$ cells were placed in 2 ml of SD media (see Yeast
889 cell culture and media) and incubated with shaking at 30 °C for 30 min. Then 1 ml of cell culture
890 was placed in Oxygraph+ system (Hansatech Instruments) and oxygen consumption was measured
891 for 4 min from each strain. As a control 10 µM of mitochondrial respiration inhibitor carbonyl
892 cyanide 3-chlorophenylhydrazone CCCP was added at the end of the measurement to account for
893 false positive signal. In total two biological replicates were used for each strain.
894
895 **Quantification and statistical analyses**
896 *LiP-MS*
897 Pairwise comparisons were performed between two conditions (young and aged), for PK-treated
898 and control (non-PK) samples respectively. Peptide (PK samples) and protein (control samples)
899 fold changes were calculated using three biological replicates per condition where the statistical
900 significance was assessed with a two-tailed heteroscedastic Student's t test. A fold change was
901 considered significant with a q-value (FDR-corrected p-value) < 0.05 for peptides and proteins [91].
902 To correct for protein abundance changes, a normalization factor based on q-value filtered protein
903 fold change for each protein was applied on corresponding peptide intensities. After correction,
904 prefiltered peptides with an absolute abundance change > 5 were selected as
905 candidates. Functional enrichment by overexpression analysis of significant LiP hits were done
906 with clusterProfiler v4.0.0 in R 4.1.0.
907
908 *Analysis of characteristics enriched among age-altered proteins*
909 Most parameters for characterization of age-altered proteins were extracted from previously
910 collected datasets described in [92]. Specifically, information about protein-protein interactions were
911 obtained from BioGRID database [93], number of GO functions retrieved through GO Slim
912 annotations [92], protein complex network using physical interactome map of yeast [94], mutation rate
913 from whole genome sequencing [95], protein abundance were obtained from cells grown in log-phase
914 and rich media from GFP signal of endogenously GFP-tagged proteins [96] and translation rate as a

bioRxiv preprint doi: https://doi.org/10.1101/2023.01.23.524173; this version posted January 23, 2023. The copyright holder for this preprint (which was not certified by peer review) is the author/funder. All rights reserved. No reuse allowed without permission.

915 function of ribosome density and occupancy [97]. The lists of anti-longevity genes of *C. elegans* and
916 *S. cerevisiae* were obtained from GenAge database [98] and the yeast list was supplemented with
917 genes identified in [99]. Statistical significance for these comparisons was assessed by unpaired t-test
918 with Welch correction with False Discovery Rate (FDR) for multiple discoveries. Effect size is
919 displayed as common language effect size (CLES). Information about protein solubility were
920 obtained from SILAC based MS measurements [100], aggregation during heat stress [44], stress granule
921 formation from affinity purification [101], asymmetrically retained long-lived proteins and their
922 fragments (LARPs) from stable-isotope pulse-chase and total proteome MS [45], essential genes from
923 growth of deletion strains in rich medium [102] and proteins with PEST motifs were predicted using
924 EMBOSS 6.5.7 [92]. Age-altered and background proteins were categorized with these
925 characteristics by constructing contingency tables. The sample size n for individual comparisons
926 between age altered proteins (N = 468) and background proteins (N = 2365) varies depending on
927 data availability. Statistical significance for contingency tables was assessed with Fisher´s exact
928 test and effect size is displayed as odds ratio (OR). Outliers were determined with Robust
929 regression and outlier removal (ROUT) test (Q = 1%).
930
931 *Microscopy image analyses*
932 Imaging data was analyzed with FIJI ImageJ software. MitoLoc analysis was performed using
933 Yeast correlation plugin [64]. Statistical significance in various images was calculated using
934 GraphPad software. Two tailed unpaired t-test was used to assess statistical significance between
935 two different groups. Ordinary one-way ANOVA with Dunnett´s correction for multiple
936 comparisons was used to assess statistical significance for number of Glt1 polymers in different
937 conditions. Two-way or three-way ANOVA with Šidák´s correction for multiple comparisons was
938 used to assess statistical significance of mitochondrial function in young and aged WT and *GLT1-*
939 *MUT* in different conditions. Correlation coefficient (R) and its significance for mitochondrial
940 function dependance on age was computed with standard Pearson´s correlation test.
941
942 *Metabolomics*
943 Peak intensity values were analyzed with Metaboanalyst software. Data was log2 transformed and
944 Pareto scaled for principal component (PCA) and orthogonal partial least square (OPLS) analyses.
945 Statistical comparison of metabolite peak intensities between WT and *GLT1-MUT* was done with
946 one-way ANOVA with Dunnett´s correction for multiple comparisons using GraphPad v9
947 software.
948
949 *RNA-seq data analysis*
950 Quality control of raw reads were performed with FastQC v0.11.9, followed by read filtering with
951 Trim Galore v0.6.6 and rRNA removal with SortMeRNA v4.2.0. Transcriptome mapping was
952 done with Salmon v1.4.0 and quality control of read mapping was done with STAR v2.7.8a and
953 Qualimap v2.2.2d. Summary of quality control results was reported with MultiQC v1.9.
954 Differentially expressed genes between young and aged cells as well as between WT and *GLT1-*
955 *MUT* cells were found using DESeq2 v1.32.0 (adjusted p-value < 0.05, Wald test) in R 4.1.0.
956 Functional enrichment of differentially expressed genes by overrepresentation analysis was done
957 with clusterProfiler v4.0.0. For this study, the yeast genome/transcriptome references and gene
958 annotations from Ensembl release 103 were used, which are based on yeast S288C genome
959 assembly R64-1-1.
960
961
962

bioRxiv preprint doi: https://doi.org/10.1101/2023.01.23.524173; this version posted January 23, 2023. The copyright holder for this preprint (which was not certified by peer review) is the author/funder. All rights reserved. No reuse allowed without permission.

Data availability

The LiP-MS proteomics, transcriptomics and metabolomics data generated and analyzed in the this study are available in the Harvard Dataverse repository (https://dataverse.harvard.edu/privateurl.xhtml?token=d4325d32-19dc-473a-952a-359b2ad668cb). All other data are included within the Article and its Extended Data.

Code availability

None of previously unreported custom code was generated in this study. Code used for processing of RNA sequencing data can be found in Harvard Dataverse depository (https://dataverse.harvard.edu/privateurl.xhtml?token=d4325d32-19dc-473a-952a-359b2ad668cb).

Acknowledgments: We thank the members of the Saarikangas lab and Jette Lengefeld for input and Cory Dunn, Markus Ralser, Ahmad Khalil and Daniel Gottschling for reagents. We are grateful to the assisting personnel at the Light Microscopy (LMU), Electron Microscopy (EMBI) and Viikki Flow Cytometry FIMM Genomics and DNA sequencing and Genomics (BIDGEN) units and MIBS and BI Media Kitchens at the University of Helsinki. Graphics in Fig. 1A and Fig. 4B, Fig. S9B were made in ©BioRender - biorender.com. This work was supported by the University of Helsinki, the Academy of Finland (317038), Sigrid Jusélius Foundation, the Human Frontiers Science Program Young Investigator Grant (RGY0080/2020) and Doctoral Programme in Integrative Life Science.

Author contributions: Conceptualization: JuS, YB, PP, JP. Methodology: JP, RMLC, YF, KT, DS, EE, PG, MD, MS, JeS, AL, JJ, HV, AN. Investigation: JP, RMLC, YF, KT, DS, EE, PG, MD, MS, AL, JH, JuS. Funding acquisition: JuS. Supervision: PT, LH, EJ, AK, PLS, VH, PP, YB, JuS. Writing - original draft: JP, JS with feedback from all the authors.

Declaration of interests: P.P. is a scientific advisor for the company Biognosys AG (Zurich, Switzerland) and PP and YF are inventors of a patent licensed by Biognosys AG that covers the LiP-MS method used in this manuscript.

Supplemental information:

Supplemental figures S1 to S9

Movie S1

bioRxiv preprint doi: https://doi.org/10.1101/2023.01.23.524173; this version posted January 23, 2023. The copyright holder for this preprint (which was not certified by peer review) is the author/funder. All rights reserved. No reuse allowed without permission.

1002

1003 # Supplemental information for

1004

1005 ## Global mapping of protein structural changes

1006 ## identifies new determinants of aging

1007

1008

1009 Jurgita Paukštytė[1,2], Rosa María López Cabezas[1,2], Yuehan Feng[3], Kai Tong[1,2,4,5], Daniela
1010 Schnyder[3], Ellinoora Elomaa[1,2], Pavlina Gregorova[2], Matteo Doudin[1,2], Meeri Särkkä[1,2], Jesse
1011 Sarameri[1,2], Alice Lippi[6], Helena Vihinen[7], Juhana Juutila[2,7], Anni Nieminen[2,7], Petri Törönen[2,7],
1012 Liisa Holm[2,7], Eija Jokitalo[7], Anita Krisko[6], Juha Huiskonen[7], L. Peter Sarin[2], Ville Hietakangas[2,7],
1013 Paola Picotti[3,8], Yves Barral[3], Juha Saarikangas[1,2,7,9,*]
1014

1015

1016 Correspondence to: juha.saarikangas@helsinki.fi
1017

1018 Supplemental Figs. S1 to S9
1019 Captions for Movie S1
1020

1021 **Other Supplemental Materials for this manuscript include the following:**
1022

1023 Movie S1
1024
1025
1026

bioRxiv preprint doi: https://doi.org/10.1101/2023.01.23.524173; this version posted January 23, 2023. The copyright holder for this preprint (which was not certified by peer review) is the author/funder. All rights reserved. No reuse allowed without permission.

1027 **Supplemental figure legends**

1028

1029 **Figure S1. Age-related structural changes are prevalent in abundant and pleiotropic**
1030 **regulators of metabolism.**
1031 **A.** Overview of the online ProtAge database containing all age-altered proteins found at
1032 https://protage-server-21.it.helsinki.fi/.
1033 **B.** Number of link communities in protein-protein interaction (PPI) network between age-altered
1034 proteins ($n = 460$) (light blue) and unaltered proteins ($n = 2279$) (grey).
1035 **C.** Fraction of essential genes among age-altered proteins ($n = 468$) (light blue) compared to
1036 unaltered proteins ($n = 2332$) (grey).
1037 **D**. Mutation rates expressed as density of amino acid substitutions between age-altered protein
1038 coding genes ($n = 417$) (light blue) and unaltered ($n = 2198$) (grey).
1039 **E.** Distribution of protein solubility between age-altered proteins ($n = 383$) (light blue) and
1040 unaltered proteins ($n = 922$) (grey).
1041 **F.** Comparison of protein abundance expressed as copy numbers per cell between between age-
1042 altered proteins (light blue) ($n = 361$) and unaltered proteins ($n = 1572$) (grey).
1043 **G.** Relative translation rate of age-altered proteins ($n = 444$) (light blue) and unaltered proteins (n
1044 $= 2162$) (grey).
1045 **H.** Fraction of proteins with protein degradation PEST motif between age-altered proteins ($n =$
1046 468) (light blue) and unaltered proteins ($n = 2332$) (grey). Black line in box plots in (B, D, F, G)
1047 is median and whiskers mark 10 and 90 percentile values. Effect size is displayed as common
1048 language effect size (CLES) (B, D, F, G), and as odds ratio (OR) (C, E, H). *$P < 0.05$; ****$P <$
1049 0.0001.

1050

1051 **Figure S2. Mapping aging-associated structural changes in the substrate-binding domain of**
1052 **Hsp70 chaperones.**
1053 **A.** Interconnected network among age-altered regulators of protein folding GO category. The
1054 graph depicts high confidence protein-protein interactions (STRING, confidence score > 0.7).
1055 **B.** Cartoon representation of ATP-bound 'closed' Hsp70. The close-up displays the Lip-peptides
1056 in Ssa1 (red) located in the nucleotide binding domain (NBD) (gray) (PDB:4B9Q; [74]).
1057 **C.** Ssb1 LiP-peptides (red) that localize in the substrate binding domain (SBD) of client peptide
1058 (yellow)-bound Hsp70 (PDB:1DKX) [49].
1059 **D.** Chordplot illustration based on (PDB:1DKX) [49] of contacts between Ssb1 LiP-peptides (red)
1060 and client peptide (yellow). Contacting secondary structures are illustrated by inner arcs.
1061 **E.** Ssb2 LiP-peptides (red) localizing in the substrate binding domain (SBD) of client peptide
1062 (yellow)-bound Hsp70 (PDB:1DKX) [49].
1063 **F.** Chordplot illustration based on (PDB:1DKX) [49] of contacts between Ssb2 LiP-peptides (red)
1064 and client peptide (yellow). Contacting secondary structures are illustrated by inner arcs.
1065 **G**. Kar2 LiP-peptides (red) localizing to substrate binding domain (SBD) of client peptide
1066 (yellow)-bound Hsp70 (PDB:1DKX) [49].
1067 **H.** Chordplot illustration based on (PDB:1DKX) [49] of contacts between Kar2 LiP-peptides (red)
1068 and client peptide (yellow). Contacting secondary structures are illustrated by inner arcs.

1069

1070 **Figure S3. Age-related structural change maps to conserved methyl donor-binding site of**
1071 **Trm1.**
1072 **A.** Protein sequence alignment between *Pyrococcus horikoshii*, *Saccharomyces cerevisiae* and
1073 *Homo sapiens* shows high conservation in the Motif II region where LiP-peptide is located. Stars
1074 mark critical residues (Ile79 and Asp78) for methyl donor binding.

bioRxiv preprint doi: https://doi.org/10.1101/2023.01.23.524173; this version posted January 23, 2023. The copyright holder for this preprint (which was not certified by peer review) is the author/funder. All rights reserved. No reuse allowed without permission.

1075 **B.** Illustration of Trm1 mediated N2,N2-dimethylguanosine ($m^2,^2G$) modification at a position G_{26}
1076 in tRNAs.
1077
1078 **Figure S4. Microscopic evaluation of amino acid synthesizing enzymes identifies age-related**
1079 **polymerization of glutamate synthase Glt1.**
1080 **A.** Enrichment map of overrepresentation of age-altered proteins in amino acid metabolism. The
1081 size of dots represents the number of proteins for every group. The color change from blue to red
1082 signify the size of an adjusted p value (p.adj. < 0.05).
1083 **B.** GFP-tagged amino acid metabolizing enzymes (green) that appeared soluble and showed no
1084 visible localization changes with age. Cell age in (B-D) can be determined from bud scars on cell
1085 wall stained with calcofluor (magenta). Scale bar 1 µm.
1086 **C.** GFP-tagged amino acid metabolizing enzymes (green) that showed punctate appearance. Scale
1087 bar 1 µm.
1088 **D.** Quantification of Glt1 polymers in aged cells (4 – 6 divisions) when tagged with either GFP or
1089 mKate2 (monomeric) fluorophores. Number of polymers displayed as mean ± SD. $n_{(GFP)} = 82$,
1090 $n_{(mKate2)} = 36$.
1091 **E.** Representative image of aged cells expressing Glt1-GFP (green) and Hsp104-mCherry (red)
1092 show no colocalization between Glt1 polymers (arrowhead) and age-associated aggregates. 52
1093 cells were examined, and none displayed accumulation of Hsp104-mCherry in Glt1 polymers.
1094 Scale bar 2 µm.
1095
1096 **Figure S5. Surface exposed hydrophobic residues mediate Glt1 self-assembly.**
1097 **A.** Quantification of cells with Glt1 polymers in normal (2% glucose (glc)) and glucose limitation
1098 (0.1% glc) conditions in synthetic complete media. Error bars represent mean ± SD from 3
1099 biological replicates. *n* = 452 for each group.
1100 **B.** Quatification of cells with Glt1 polymers in SD medium containing 5 g/L of $(NH_4)_2SO_4$ as high
1101 nitrogen (high NH_4) conditions or SD medium with twice less of yeast nitrogen base (YNB) as low
1102 nitrogen (low NH_4) conditions. $n_{SD} = 558$, $n_{High\ NH4} = 164$, $n_{Low\ NH4} = 214$ from three biological
1103 replicates.
1104 **C.** Validation of the effect of mutagenesis on Glt1 self-assembly. Representative images of Glt1
1105 mutant cells. Calcofluor marks the cell wall (magenta). Scale bar 1 µm.
1106 **D.** Western blot analysis of expression levels of Glt1 mutant proteins. Glt1-GFP was detected with
1107 anti-GFP antibody (band size 265 kDa). Antibody against Pgk1 (45 kDa) was used as a loading
1108 control.
1109 **E.** Quantification of relative band intensity of Glt1 mutant M3 (*GLT1-MUT*) to the WT. Bands
1110 were normalized to the band intensity of loading control. *n* = 2.
1111 **F.** Schematic overview of L-glutamate synthesis in yeast which relies on two pathways: glutamate
1112 synthase Glt1 and glutamate dehydrogenases Gdh1 and Gdh3.
1113 **G.** Catalytic activity of Glt1 mutant M3 (*GLT1-MUT*) was evaluated by growth essay on media
1114 without glutamate in strains that were deleted of *GDH1* and *GDH3*. Glt1 mutant M3 (*GLT1-MUT*)
1115 rescues the growth defect observed in a triple deletion (Δg*dh1* Δ*gdh3* Δ*glt1*) in a comparable
1116 manner as WT Glt1.
1117 **H.** Localization of LiP-peptides in the cartoon model of Glt1 hexamer with dihedral symmetry
1118 (D3) and putative assembly mechanism.
1119 **I.** Localization of LiP-peptides in the cartoon model of Glt1 trimer with cyclic symmetry (C3) and
1120 putative assembly mechanism. Error bars represent mean ± SD. Significance of the difference in
1121 A-B, E) was assessed with unpaired two-tailed t test assuming equal variance. n.s. not significant.
1122

bioRxiv preprint doi: https://doi.org/10.1101/2023.01.23.524173; this version posted January 23, 2023. The copyright holder for this preprint (which was not certified by peer review) is the author/funder. All rights reserved. No reuse allowed without permission.

1123 **Figure S6. Glt1 polymerization mediates transcriptional changes in aged cells.**
1124 **A.** Table summarizing number of genes with significantly age-altered expression levels between
1125 WT and *GLT1-MUT* cells Significance of differential expression was statistically evaluated with
1126 Wald test. (P adjusted < 0.05), $n = 4$.
1127 **B.** GO enrichment by over-representation analysis between aged WT and *GLT1-MUT* cells
1128 showing enriched biological process in which gene expression was altered when polymerization
1129 of Glt1 is engaged. The size of dots represents the number of proteins for every biological process.
1130 The color change from blue to red signify the size of an adjusted p value (P adjusted < 0.05).
1131
1132 **Figure S7. Glt1 polymerization results in increased glutamine uptake in aged WT cells.**
1133 **A.** Cell size distribution among aged cells with or without their budding daughters between WT
1134 and *GLT1-MUT*. Number of cells analyzed: aged mother cells $n = 84$, aged mother cells with their
1135 budding daughters $n_{WT} = 138$ $n_{GLT1\text{-}MUT} = 130$.
1136 **B.** Vacuolar pH in WT and *GLT1-MUT* cells in the presence or absence of 500 nM of concA
1137 measured by flow cytometry in cells stained with 50 µM of 2′,7′-Bis(2-carboxyethyl)-5(6)-
1138 carboxyfluorescein acetoxymethyl ester (BCECF/AM). Biological replicates $n = 3$, analyzed
1139 cells per sample $n \geq 10000$.
1140 **C.** Quantification of cells with Glt1 polymers in the presence or absence of 500 nM
1141 concanamycin A (concA). Error bars represent mean ± SD from 3 biological replicates. $n_{SD} =$
1142 339, $n_{SD\ concA} = 366$.
1143 **D.** Schematic overview of labelled $^{13}C_5$-$^{15}N_2$-glutamine incorporation into cell metabolism.
1144 Labelled glutamine (Gln) taken up by cells is used for glutamate (Glu) production by Glt1 and
1145 Gdh1 and Gdh3. Glutamate can be further used for glutamine and alpha-ketoglutarate (α-KG)
1146 synthesis or for amino acid (AA) synthesis via transamination.
1147 **E.** Fractional contribution of labelled glutamate species from Glt1 or Gdh1 and Gdh3 reactions
1148 in young and aged cells. Squares represent parts of whole of total labelled glutamate species. $n =$
1149 4.
1150 **F.** Fractional enrichment of all glutamate species in WT and *GLT1-MUT* in young and aged
1151 cells. $n = 4$.
1152 **G.** Fractional enrichment of all glutamine species in WT and *GLT1-MUT* in young and aged
1153 cells. $n = 4$. Error bars represent mean ± SD. Statistical significance in (A, C) was assessed by
1154 two-tailer unpaired t test assuming equal variance and (F-G) with ordinary one-way ANOVA
1155 with Dunnett´s correction for multiple comparisons and B with two-way ANOVA Šidák´s
1156 correction. *$P < 0.05$; **$P < 0.01$; n.s. not significant.
1157
1158 **Figure S8. Polymerization of Glt1 results in expression changes in general amino acid**
1159 **transporters.**
1160 **A.** General amino acid transporters that import glutamine Gnp1, Dip5 and Gap1 were tagged with
1161 GFP and their expression levels in young and aged cells were measured with flow cytometry.
1162 Heatmap summarizes fold change with age in WT and *GLT1-MUT* cells. Biological replicates $n =$
1163 3, analyzed cells per sample $n \geq 10\,000$.
1164 **B.** Microscopic images of Gnp1-GFP (green) in aged WT cells and *GLT1-MUT* cells. Cell age is
1165 indicated by calcofluor staining of the cell wall (magenta). Scale bar 1 µm.
1166 **C.** Quantification of GFP signal from Gnp1-GFP transporter by flow cytometry between WT and
1167 *GLT1-MUT* in young and aged cells. Error bars represent mean ± SD. Statistical significance
1168 was assessed with two-way ANOVA with Šidák´s correction for multiple comparisons.
1169 Biological replicates $n = 3$, analyzed cells per sample $n \geq 10\,000$. ****$P < 0.0001$.
1170

bioRxiv preprint doi: https://doi.org/10.1101/2023.01.23.524173; this version posted January 23, 2023. The copyright holder for this preprint (which was not certified by peer review) is the author/funder. All rights reserved. No reuse allowed without permission.

1171 **Figure S9. Glt1 polymerization is associated with mitochondrial dysfunction at early stage**
1172 **in replicative lifespan.**
1173 **A.** Probability of death comparison between WT and *GLT1-MUT* cells during the first 20 divisions.
1174 $n_{wt} = 40$, $n_{GLT1\text{-}MUT} = 62$.
1175 **B.** MitoLoc enables single-cell analysis of mitochondrial function through colocalization of
1176 mitochondrial preSU9-GFP (green) and cytosolic preCOX4-mCherry (red) signals. The import
1177 of preCOX4, but not preSU9, depends on mitochondrial membrane potential.
1178 **C.** Mitochondrial function between WT and GLT1-MUT cells was evaluated with MitoLoc
1179 construct and is displayed as a Pearson´s correlation coefficient of colocalization between
1180 mitochondrial peSU9-GFP and cytosolic preCOX4-mCherry. Non-polymerizing mutant maintain
1181 stable mitochondrial function during the early stage of replicative life span (4-6 divisions). $n_{WT} =$
1182 211, $n_{GLT1\text{-}MUT} = 184$.
1183 **D.** Distribution of mitochondrial morphology in young and aged WT and Glt1 mutant cells. Pie
1184 charts represent parts of whole of mitochondrial morphology distribution in group of cells. $n_{WT} =$
1185 211, $n_{GLT1\text{-}MUT} = 184$.
1186 **E.** Oxygen consumption in young and aged cells between WT and GLT1-MUT cells. Oxygen
1187 consumption was measured with oxygraph in exponentially grown culture after MACS
1188 purification of young and aged cells. $n = 3$ biological replicates.
1189 **F.** Quantification of cells with Glt1 polymers in the presence or absence of 10 μM carbonyl
1190 cyanide m-chlorophenylhydrazone (CCCP), which disrupts mitochondrial membrane potential. 3
1191 biological replicates with $n = 100$ for each group. Error bars represent mean ± SD. Statistical
1192 significance (C, E) was assessed with two-way ANOVA with Šidák´s correction for multiple
1193 comparisons. $^{**}P < 0.01$; $^{***}P < 0.001$ $^{****}P < 0.0001$; n.s. not significant.
1194

1195 **Movie S1.**
1196 Time-lapse fluorescence microscopy of dividing yeast cells expressing endogenous Glt1 tagged
1197 with GFP (green). Newly born daughter cells are born with diffuse Glt1. After a few divisions,
1198 Glt1 transitions into polymeric assembly which is asymmetrically retained in the mother cells
1199 during cell division. Images were taken every 15 min for a total period of 315 min.
1200
1201

1202 **References:**

1203 1. Jarosz, D.F., Taipale, M., and Lindquist, S. (2010). Protein homeostasis and the phenotypic
1204 manifestation of genetic diversity: Principles and mechanisms. Annu Rev Genet 44, 189–216.
1205 10.1146/annurev.genet.40.110405.090412.

1206 2. Nussinov, R., Tsai, C.J., and Jang, H. (2019). Protein ensembles link genotype to phenotype.
1207 PLoS Comput Biol 15, 1–21. 10.1371/journal.pcbi.1006648.

1208 3. Cappelletti, V., Hauser, T., Piazza, I., Caflisch, A., Souza, N. de, Picotti, P., Cappelletti, V.,
1209 Hauser, T., Piazza, I., Pepelnjak, M., et al. (2021). Dynamic 3D proteomes reveal protein
1210 functional alterations at high resolution in situ. Cell 184, 545–559.
1211 10.1016/j.cell.2020.12.021.

bioRxiv preprint doi: https://doi.org/10.1101/2023.01.23.524173; this version posted January 23, 2023. The copyright holder for this preprint (which was not certified by peer review) is the author/funder. All rights reserved. No reuse allowed without permission.

1212 4. Gnann, C., Cesnik, A.J., and Lundberg, E. (2021). Illuminating Non-genetic Cellular
1213 Heterogeneity with Imaging-Based Spatial Proteomics. Trends Cancer 7, 278–282.
1214 10.1016/j.trecan.2020.12.006.

1215 5. Tan, C.S.H., Go, K.D., Bisteau, X., Dai, L., Yong, C.H., Prabhu, N., Ozturk, M.B., Lim, Y.T.,
1216 Sreekumar, L., Lengqvist, J., et al. (2018). Thermal proximity coaggregation for system-wide
1217 profiling of protein complex dynamics in cells. Science (1979) 359, 1170–1177.
1218 10.1126/science.aan0346.

1219 6. Bludau, I., and Aebersold, R. (2020). Proteomic and interactomic insights into the molecular
1220 basis of cell functional diversity. Nat Rev Mol Cell Biol 21, 327–340. 10.1038/s41580-020-
1221 0231-2.

1222 7. Aebersold, R., Agar, J.N., Amster, I.J., Baker, M.S., Bertozzi, C.R., Boja, E.S., Costello, C.E.,
1223 Cravatt, B.F., Fenselau, C., Garcia, B.A., et al. (2018). How many human proteoforms are
1224 there? Nat Chem Biol 14, 206–214. 10.1038/nchembio.2576.

1225 8. Porter, L.L., and Looger, L.L. (2018). Extant fold-switching proteins are widespread. Proc
1226 Natl Acad Sci U S A 115, 5968–5973. 10.1073/pnas.1800168115.

1227 9. Flock, T., Weatheritt, R.J., Latysheva, N.S., and Babu, M.M. (2014). Controlling entropy to
1228 tune the functions of intrinsically disordered regions. Curr Opin Struct Biol 26, 62–72.
1229 10.1016/j.sbi.2014.05.007.

1230 10. Wright, P.E., and Dyson, H.J. (2015). Intrinsically disordered proteins in cellular signalling
1231 and regulation. Nat Rev Mol Cell Biol 16, 18–29. 10.1038/nrm3920.

1232 11. Yoo, H., Triandafillou, C., and Drummond, D.A. (2019). Cellular sensing by phase
1233 separation: Using the process, not just the products. Journal of Biological Chemistry 294,
1234 7151–7159. 10.1074/jbc.TM118.001191.

1235 12. Alberti, S., and Hyman, A.A. (2021). Biomolecular condensates at the nexus of cellular stress,
1236 protein aggregation disease and ageing. Nat Rev Mol Cell Biol 22, 196–213. 10.1038/s41580-
1237 020-00326-6.

1238 13. López-Otín, C., Blasco, M.A., Partridge, L., Serrano, M., and Kroemer, G. (2013). The
1239 hallmarks of aging. Cell 153, 1194. 10.1016/j.cell.2013.05.039.

1240 14. Dillin, A., Gottschling, D.E., and Nyström, T. (2014). The good and the bad of being
1241 connected: The integrons of aging. Curr Opin Cell Biol 26, 107–112.
1242 10.1016/j.ceb.2013.12.003.

1243 15. Denoth Lippuner, A., Julou, T., and Barral, Y. (2014). Budding yeast as a model organism to
1244 study the effects of age. FEMS Microbiol Rev 38, 300–325. 10.1111/1574-6976.12060.

bioRxiv preprint doi: https://doi.org/10.1101/2023.01.23.524173; this version posted January 23, 2023. The copyright holder for this preprint (which was not certified by peer review) is the author/funder. All rights reserved. No reuse allowed without permission.

1245 16. Knorre, D.A., Azbarova, A. V., Galkina, K. V., Feniouk, B.A., and Severin, F.F. (2018).
1246 Replicative aging as a source of cell heterogeneity in budding yeast. Mech Ageing Dev 176,
1247 24–31. 10.1016/j.mad.2018.09.001.

1248 17. Janssens, G.E., and Veenhoff, L.M. (2016). Evidence for the hallmarks of human aging in
1249 replicatively aging yeast. Microbial Cell 3, 263–274. 10.15698/mic2016.07.510.

1250 18. Neurohr, G.E., Terry, R.L., Lengefeld, J., Bonney, M., Brittingham, G.P., Moretto, F.,
1251 Miettinen, T.P., Vaites, L.P., Soares, L.M., Paulo, J.A., et al. (2019). Excessive Cell Growth
1252 Causes Cytoplasm Dilution And Contributes to Senescence. Cell 176, 1083-1097.e18.
1253 10.1016/j.cell.2019.01.018.

1254 19. Leupold, S., Hubmann, G., Litsios, A., Meinema, A.C., Takhaveev, V., Papagiannakis, A.,
1255 Niebel, B., Janssens, G., Siegel, D., and Heinemann, M. (2019). Saccharomyces cerevisiae
1256 goes through distinct metabolic phases during its replicative lifespan. Elife 8, 1–19.
1257 10.7554/eLife.41046.

1258 20. Kamei, Y., Tamada, Y., Nakayama, Y., Fukusaki, E., and Mukai, Y. (2014). Changes in
1259 transcription and metabolism during the early stage of replicative cellular senescence in
1260 budding yeast. Journal of Biological Chemistry 289, 32081–32093.
1261 10.1074/jbc.M114.600528.

1262 21. McFaline-Figueroa, J.R., Vevea, J., Swayne, T.C., Zhou, C., Liu, C., Leung, G., Boldogh,
1263 I.R., and Pon, L.A. (2011). Mitochondrial quality control during inheritance is associated with
1264 lifespan and mother-daughter age asymmetry in budding yeast. Aging Cell, 885–895.
1265 https://doi.org/10.1111/j.1474-9726.2011.00731.x.

1266 22. Hughes, A.L., and Gottschling, D.E. (2012). An early age increase in vacuolar pH limits
1267 mitochondrial function and lifespan in yeast. Nature 492, 261–265. 10.1038/nature11654.

1268 23. Li, Y., Jiang, Y., Paxman, J., Laughlin, R.O., Klepin, S., Zhu, Y., Pillus, L., Tsimring, L.S.,
1269 Hasty, J., and Hao, N. (2020). A programmable fate decision landscape underlies single-cell
1270 aging in yeast. 329, 325–329. doi: 10.1126/science.aax9552.

1271 24. Erjavec, N., Larsson, L., Grantham, J., and Nyström, T. (2007). Accelerated aging and failure
1272 to segregate damaged proteins in Sir2 mutants can be suppressed by overproducing the
1273 protein aggregation-remodeling factor Hsp104p. Genes Dev 21, 2410–2421.
1274 10.1101/gad.439307.

1275 25. Saarikangas, J., and Barral, Y. (2015). Protein aggregates are associated with replicative
1276 aging without compromising protein quality control. Elife 4, 1–24. 10.7554/eLife.06197.

1277 26. Gladyshev, V.N., Kritchevsky, S.B., Clarke, S.G., Cuervo, A.M., Fiehn, O., Magalhães, J.P.
1278 de, Mau, T., Maes, M., Moritz, R.L., Niedernhofer, L.J., et al. (2021). Molecular damage in
1279 aging. Nat Aging 1, 1096–1106. https://doi.org/10.1038/s43587-021-00150-3.

bioRxiv preprint doi: https://doi.org/10.1101/2023.01.23.524173; this version posted January 23, 2023. The copyright holder for this preprint (which was not certified by peer review) is the author/funder. All rights reserved. No reuse allowed without permission.

1280 27. Sen, P., Shah, P.P., Nativio, R., and Berger, S.L. (2016). Epigenetic Mechanisms of
1281 Longevity and Aging. Cell 166, 822–839. 10.1016/j.cell.2016.07.050.

1282 28. The Tabula Muris Consortium (2020). A single-cell transcriptomic atlas characterizes ageing
1283 tissues in the mouse. 583, 590–595. 10.1038/s41586-020-2496-1.

1284 29. Zhang, Y., Wang, J., Sang, Y., Jin, S., Wang, X., Azad, G.K., McCormick, M.A., Kennedy,
1285 B.K., Li, Q., Wang, J., et al. (2020). Single-cell RNA-seq reveals early heterogeneity during
1286 ageing in yeast. bioRxiv, 2020.09.04.282525. 10.1101/2020.09.04.282525.

1287 30. Janssens, G.E., Meinema, A.C., González, J., Wolters, J.C., Schmidt, A., Guryev, V.,
1288 Bischoff, R., Wit, E.C., Veenhoff, L.M., and Heinemann, M. (2015). Protein biogenesis
1289 machinery is a driver of replicative aging in yeast. Elife 4. 10.7554/eLife.08527.

1290 31. Martinez-Miguel, V.E., Lujan, C., Espie–Caullet, T., Martinez-Martinez, D., Moore, S.,
1291 Backes, C., Gonzalez, S., Galimov, E.R., Brown, A.E.X., Halic, M., et al. (2021). Increased
1292 fidelity of protein synthesis extends lifespan. Cell Metab 33, 2288-2300.e12.
1293 10.1016/j.cmet.2021.08.017.

1294 32. Stein, K.C., Morales-Polanco, F., van der Lienden, J., Rainbolt, T.K., and Frydman, J. (2022).
1295 Ageing exacerbates ribosome pausing to disrupt cotranslational proteostasis. Nature 601,
1296 637–642. 10.1038/s41586-021-04295-4.

1297 33. Labbadia, J., and Morimoto, R.I. (2015). The biology of proteostasis in aging and disease.
1298 Annu Rev Biochem 84, 435–464. 10.1146/annurev-biochem-060614-033955.

1299 34. Hipp, M.S., Kasturi, P., and Hartl, F.U. (2019). The proteostasis network and its decline in
1300 ageing. Nat Rev Mol Cell Biol 20, 421–435. 10.1038/s41580-019-0101-y.

1301 35. Shuken, S.R., Rutledge, J., Iram, T., Losada, P.M., Wilson, E.N., Andreasson, K.I., Leib,
1302 R.D., and Wyss-Coray, T. (2022). Limited proteolysis–mass spectrometry reveals aging-
1303 associated changes in cerebrospinal fluid protein abundances and structures. Nat Aging 2,
1304 379–388. 10.1038/s43587-022-00196-x.

1305 36. David, D.C., Ollikainen, N., Trinidad, J.C., Cary, M.P., Burlingame, A.L., and Kenyon, C.
1306 (2010). Widespread protein aggregation as an inherent part of aging in C. elegans. PLoS Biol
1307 8, 47–48. 10.1371/journal.pbio.1000450.

1308 37. Chen, Y.R., Harel, I., Singh, P.P., Ziv, I., Moses, E., Goshtchevsky, U., Machado, B.E.,
1309 Brunet, A., and Jarosz, D.F. (2022). Tissue-specific landscape of protein aggregation and
1310 quality control in an aging vertebrate. bioRxiv, 2022.02.26.482120.
1311 10.1101/2022.02.26.482120.

1312 38. Soto, C., and Pritzkow, S. (2018). Protein misfolding, aggregation, and conformational strains
1313 in neurodegenerative diseases. Nat Neurosci 21. 10.1038/s41593-018-0235-9.

bioRxiv preprint doi: https://doi.org/10.1101/2023.01.23.524173; this version posted January 23, 2023. The copyright holder for this preprint (which was not certified by peer review) is the author/funder. All rights reserved. No reuse allowed without permission.

1314 39. Henderson, K.A., and Gottschling, D.E. (2008). A mother's sacrifice: what is she keeping for
1315 herself? Curr Opin Cell Biol 20, 723–728. 10.1016/j.ceb.2008.09.004.

1316 40. Feng, Y., De Franceschi, G., Kahraman, A., Soste, M., Melnik, A., Boersema, P.J., De
1317 Laureto, P.P., Nikolaev, Y., Oliveira, A.P., and Picotti, P. (2014). Global analysis of protein
1318 structural changes in complex proteomes. Nat Biotechnol 32, 1036+. 10.1038/nbt.2999.

1319 41. Schopper, S., Kahraman, A., Leuenberger, P., Feng, Y., Piazza, I., Müller, O., Boersema, P.J.,
1320 and Picotti, P. (2017). Measuring protein structural changes on a proteome-wide scale using
1321 limited proteolysis-coupled mass spectrometry. Nat Protoc 12, 2391–2410.
1322 10.1038/nprot.2017.100.

1323 42. Leuenberger, P., Ganscha, S., Kahraman, A., Cappelletti, V., Boersema, P.J., Von Mering,
1324 C., Claassen, M., and Picotti, P. (2017). Cell-wide analysis of protein thermal unfolding
1325 reveals determinants of thermostability. Science (1979) 355. 10.1126/science.aai7825.

1326 43. Jumper, J., Evans, R., Pritzel, A., Green, T., Figurnov, M., Ronneberger, O.,
1327 Tunyasuvunakool, K., Bates, R., Žídek, A., Potapenko, A., et al. (2021). Highly accurate
1328 protein structure prediction with AlphaFold. Nature 596, 583–589. 10.1038/s41586-021-
1329 03819-2.

1330 44. Wallace, E.W.J., Kear-Scott, J.L., Pilipenko, E. V., Schwartz, M.H., Laskowski, P.R., Rojek,
1331 A.E., Katanski, C.D., Riback, J.A., Dion, M.F., Franks, A.M., et al. (2015). Reversible,
1332 Specific, Active Aggregates of Endogenous Proteins Assemble upon Heat Stress. Cell 162,
1333 1286–1298. 10.1016/j.cell.2015.08.041.

1334 45. Thayer, N.H., Leverich, C.K., Fitzgibbon, M.P., Nelson, Z.W., Henderson, K.A., Gafken,
1335 P.R., Hsu, J.J., and Gottschling, D.E. (2014). Identification of long-lived proteins retained in
1336 cells undergoing repeated asymmetric divisions. Proceedings of the National Academy of
1337 Sciences 111, 14019–14026. 10.1073/pnas.1416079111.

1338 46. Sontag, E.M., Samant, R.S., and Frydman, J. (2017). Mechanisms and functions of ribosome-
1339 associated protein quality control. Annual Review of BiochemistryBiochemistry, 97–122.
1340 10.1038/s41580-019-0118-2.

1341 47. Moreno, D.F., Jenkins, K., Morlot, S., Charvin, G., Csikasz-Nagy, A., and Aldea, M. (2019).
1342 Proteostasis collapse, a hallmark of aging, hinders the chaperone-start network and arrests
1343 cells in G1. Elife 8, 1–27. 10.7554/eLife.48240.

1344 48. Rosenzweig, R., Nillegoda, N.B., Mayer, M.P., and Bukau, B. (2019). The Hsp70 chaperone
1345 network. Nat Rev Mol Cell Biol 20, 665–680. 10.1038/s41580-019-0133-3.

1346 49. Zhu, X., Zhao, X., Burkholder, W.F., Gragerov, A., Ogata, C.M., Gottesman, M.E., and
1347 Hendrickson, W.A. (1996). Structural analysis of substrate binding by the molecular
1348 chaperone DnaK. Science (1979) 272, 1606–1614. 10.1126/science.272.5268.1606.

bioRxiv preprint doi: https://doi.org/10.1101/2023.01.23.524173; this version posted January 23, 2023. The copyright holder for this preprint (which was not certified by peer review) is the author/funder. All rights reserved. No reuse allowed without permission.

1349 50. Kayikci, M., Venkatakrishnan, A.J., Scott-Brown, J., Ravarani, C.N.J., Flock, T., and Babu,
1350 M.M. (2018). Visualization and analysis of non-covalent contacts using the Protein Contacts
1351 Atlas. Nat Struct Mol Biol 25, 185–194. 10.1038/s41594-017-0019-z.

1352 51. Nedialkova, D.D., and Leidel, S.A. (2015). Optimization of Codon Translation Rates via
1353 tRNA Modifications Maintains Proteome Integrity. Cell 161, 1606–1618.
1354 10.1016/j.cell.2015.05.022.

1355 52. Ihsanawati, Nishimoto, M., Higashijima, K., Shirouzu, M., Grosjean, H., Bessho, Y., and
1356 Yokoyama, S. (2008). Crystal Structure of tRNA N2,N2-Guanosine Dimethyltransferase
1357 Trm1 from Pyrococcus horikoshii. J Mol Biol 383, 871–884. 10.1016/j.jmb.2008.08.068.

1358 53. Noree, C., Sato, B.K., Broyer, R.M., and Wilhelm, J.E. (2010). Identification of novel
1359 filament-forming proteins in Saccharomyces cerevisiae and Drosophila melanogaster. J Cell
1360 Biol 190, 541–551. 10.1083/jcb.201003001.

1361 54. O'Connell, J.D., Tsechansky, M., Royall, A., Boutz, D.R., Ellington, A.D., and Marcotte,
1362 E.M. (2014). A proteomic survey of widespread protein aggregation in yeast. Mol Biosyst
1363 10, 851–861. 10.1039/c3mb70508k.

1364 55. Petrovska, I., Nüske, E., Munder, M.C., Kulasegaran, G., Malinovska, L., Kroschwald, S.,
1365 Richter, D., Fahmy, K., Gibson, K., Verbavatz, J.M., et al. (2014). Filament formation by
1366 metabolic enzymes is a specific adaptation to an advanced state of cellular starvation. Elife
1367 2014, 1–19. 10.7554/eLife.02409.

1368 56. Shen, Q.J., Kassim, H., Huang, Y., Li, H., Zhang, J., Li, G., Wang, P.Y., Yan, J., Ye, F., and
1369 Liu, J.L. (2016). Filamentation of Metabolic Enzymes in Saccharomyces cerevisiae. Journal
1370 of Genetics and Genomics 43, 393–404. 10.1016/j.jgg.2016.03.008.

1371 57. Cottevieille, M., Larquet, E., Jonic, S., Petoukhov, M. V., Caprini, G., Paravisi, S., Svergun,
1372 D.I., Vanoni, M.A., and Boisset, N. (2008). The subnanometer resolution structure of the
1373 glutamate synthase 1.2-MDa hexamer by cryoelectron microscopy and its oligomerization
1374 behavior in solution: Functional implications. Journal of Biological Chemistry 283, 8237–
1375 8249. 10.1074/jbc.M708529200.

1376 58. Garcia-Seisdedos, H., Empereur-Mot, C., Elad, N., and Levy, E.D. (2017). Proteins evolve
1377 on the edge of supramolecular self-assembly. Nature 548, 244–247. 10.1038/nature23320.

1378 59. Park, C.K., and Horton, N.C. (2019). Structures, functions, and mechanisms of filament
1379 forming enzymes: a renaissance of enzyme filamentation. Biophys Rev 11, 927–994.
1380 10.1007/s12551-019-00602-6.

1381 60. Montrose, K., Lopez Cabezas, R.M., Paukstyte, J., and Saarikangas, J. (2020). Winter is
1382 coming : Regulation of cellular metabolism by enzyme polymerization in dormancy and
1383 disease. Exp Cell Res 397. 10.1016/j.yexcr.2020.112383.

bioRxiv preprint doi: https://doi.org/10.1101/2023.01.23.524173; this version posted January 23, 2023. The copyright holder for this preprint (which was not certified by peer review) is the author/funder. All rights reserved. No reuse allowed without permission.

1384 61. Hughes, C.E., Coody, T.K., Jeong, M.Y., Berg, J.A., Winge, D.R., and Hughes, A.L. (2020).
1385 Cysteine Toxicity Drives Age-Related Mitochondrial Decline by Altering Iron Homeostasis.
1386 Cell 180, 296-310.e18. 10.1016/j.cell.2019.12.035.

1387 62. Zhu, X., Garrett, J., Schreve, J., and Michaeli, T. (1996). GNP1, the high affinity glutamine
1388 permease of S. cerevisiae. Curr Genet 30, 107–114. 10.1007/s002940050108.

1389 63. Kaya, A., Phua, C.Z.J., Lee, M., Wang, L., Tyshkovskiy, A., Ma, S., Barre, B., Liu, W.,
1390 Harrison, B.R., Zhao, X., et al. (2021). Evolution of natural lifespan variation and molecular
1391 strategies of extended lifespan in yeast. Elife 10, 1–28. 10.7554/eLife.64860.

1392 64. Vowinckel, J., Hartl, J., Butler, R., and Ralser, M. (2015). MitoLoc: A method for the
1393 simultaneous quantification of mitochondrial network morphology and membrane potential
1394 in single cells. Mitochondrion 24, 77–86. 10.1016/j.mito.2015.07.001.

1395 65. Schlissel, G., Krzyzanowski, M.K., Caudron, F., Barral, Y., and Rine, J. (2017). Aggregation
1396 of the Whi3 protein, not loss of heterochromatin, causes sterility in old yeast cells. Science
1397 (1979) 355, 1184–1187. 10.1126/science.aaj2103.

1398 66. Garcia-Seisdedos, H., Villegas, J.A., and Levy, E.D. (2019). Infinite Assembly of Folded
1399 Proteins in Evolution, Disease, and Engineering. Angewandte Chemie - International Edition
1400 58, 5514–5531. 10.1002/anie.201806092.

1401 67. Mouton, S.N., Thaller, D.J., Crane, M.M., Rempel, I.L., Terpstra, O.T., Steen, A., Kaeberlein,
1402 M., Lusk, C.P., Boersma, A.J., and Veenhoff, L.M. (2020). A physicochemical perspective
1403 of aging from single-cell analysis of pH , macromolecular and organellar crowding in yeast.
1404 Elife, e54707. https://doi.org/10.7554/elife.54707.

1405 68. Correia-Melo, C., Kamrad, S., Messner, C.B., Tengölics, R., Herrera-Dominguez, L.,
1406 Townsend, S.J., Alam, M.T., Freiwald, A., Campbell, K., Aulakh, S., et al. (2022). Cell-cell
1407 metabolite exchange creates a pro-survival metabolic environment that extends lifespan.
1408 bioRxiv, 2022.03.07.483228. 10.1101/2022.03.07.483228.

1409 69. Clay, L., Caudron, F., Denoth-Lippuner, A., Boettcher, B., Frei, S.B., Snapp, E.L., and Barral,
1410 Y. (2014). A sphingolipid-dependent diffusion barrier confines ER stress to the yeast mother
1411 cell. Elife 2014, 1–23. 10.7554/eLife.01883.

1412 70. Santra, M., Dill, K.A., and De Graff, A.M.R. (2019). Proteostasis collapse is a driver of cell
1413 aging and death. Proc Natl Acad Sci U S A 116, 22173–22178. 10.1073/pnas.1906592116.

1414 71. Colman-lerner, A., Chin, T.E., and Brent, R. (2001). Yeast Cbk1 and Mob2 Activate
1415 Daughter-Specific Genetic Programs to Induce Asymmetric Cell Fates. 107, 739–750.
1416 https://doi.org/10.1016/s0092-8674(01)00596-7.

1417 72. Ghaemmaghami, S., Huh, W.K., Bower, K., Howson, R.W., Belle, A., Dephoure, N., O'Shea,
1418 E.K., and Weissman, J.S. (2003). Global analysis of protein expression in yeast. Nature 425,
1419 737–741. 10.1038/nature02046.

bioRxiv preprint doi: https://doi.org/10.1101/2023.01.23.524173; this version posted January 23, 2023. The copyright holder for this preprint (which was not certified by peer review) is the author/funder. All rights reserved. No reuse allowed without permission.

73. Thul, P.J., Akesson, L., Wiking, M., Mahdessian, D., Geladaki, A., Ait Blal, H., Alm, T., Asplund, A., Björk, L., Breckels, L.M., et al. (2017). A subcellular map of the human proteome. Science (1979) 356, eaal3321. 10.1126/science.aal3321.

74. Bertelsena, E.B., Chang, L., Gestwicki, J.E., and Zuiderweg, E.R.P. (2009). Solution conformation of wild-type E. coli Hsp70 (DnaK) chaperone complexed with ADP and substrate. Proc Natl Acad Sci U S A 106, 8471–8476. 10.1073/pnas.0903503106.

75. Brachmann, C.B., Davies, A., Cost, G.J., Caputo, E., Li, J., Hieter, P., and Boeke, J.D. (1998). Designer deletion strains derived from Saccharomyces cerevisiae S288C: A useful set of strains and plasmids for PCR-mediated gene disruption and other applications. Yeast 14, 115–132. 10.1002/(SICI)1097-0061(19980130)14:2<115::AID-YEA204>3.0.CO;2-2.

76. Lindstrom, D.L., and Gottschling, D.E. (2009). The mother enrichment program: A genetic system for facile replicative life span analysis in Saccharomyces cerevisiae. Genetics 183, 413–422. 10.1534/genetics.109.106229.

77. Lequin, S., Chassagne, D., Bellat, J.-P., Huh, W., Falvo, J. V, Gerke, L.C., Carroll, A.S., Howson, R.W., Weissman, J.S., and Shea, E.K.O. (2003). Global analysis of protein localization in budding yeast. Nature 425, 686–691. 10.1038/nature02026.

78. Winzeler, E.A., Shoemaker, D.D., Astromoff, A., Liang, H., Anderson, K., Andre, B., Bangham, R., Benito, R., Boeke, J.D., Bussey, H., et al. (1999). Functional characterization of the S. cerevisiae genome by gene deletion and parallel analysis. Science (1979) 285, 901–906. 10.1126/science.285.5429.901.

79. Janke, C., Magiera, M.M., Rathfelder, N., Taxis, C., Reber, S., Maekawa, H., Moreno-Borchart, A., Doenges, G., Schwob, E., Schiebel, E., et al. (2004). A versatile toolbox for PCR-based tagging of yeast genes: New fluorescent proteins, more markers and promoter substitution cassettes. Yeast 21, 947–962. 10.1002/yea.1142.

80. Newby, G.A., Kiriakov, S., Hallacli, E., Liebman, S.W., Lindquist, S., Khalil, A.S., Newby, G.A., Kiriakov, S., Hallacli, E., Kayatekin, C., et al. (2017). Resource A Genetic Tool to Track Protein Aggregates and Control Prion Inheritance Resource A Genetic Tool to Track Protein Aggregates and Control Prion Inheritance. Cell, 1–14. 10.1016/j.cell.2017.09.041.

81. Laughery, M.F., Shumaker, T., Hunter, T., Brown, A., Hoopes, J., Ostbye, T., and Wyrick, J.J. (2015). New Vectors for Simple and Streamlined CRISPR-Cas9 Genome Editing in Saccharomyces cerevisiae. Yeast 32, 711–720. 10.1002/yea.3098.New.

82. Huang, F., Spangler, J.R., and Huang, A.Y. (2017). In vivo cloning of up to 16 kb plasmids in E. coli is as simple as PCR. PLoS One 12, 1–21. 10.1371/journal.pone.0183974.

83. Pettersen, E.F., Goddard, T.D., Huang, C.C., Meng, E.C., Couch, G.S., Croll, T.I., Morris, J.H., and Ferrin, T.E. (2021). UCSF ChimeraX: Structure visualization for researchers, educators, and developers. Protein Science 30, 70–82. 10.1002/pro.3943.

bioRxiv preprint doi: https://doi.org/10.1101/2023.01.23.524173; this version posted January 23, 2023. The copyright holder for this preprint (which was not certified by peer review) is the author/funder. All rights reserved. No reuse allowed without permission.

1456 84. Goddard, T.D., Huang, C.C., Meng, E.C., Pettersen, E.F., Couch, G.S., Morris, J.H., and
1457 Ferrin, T.E. (2018). UCSF ChimeraX: Meeting modern challenges in visualization and
1458 analysis. Protein Science 27, 14–25. 10.1002/pro.3235.

1459 85. Kityk, R., Kopp, J., Sinning, I., and Mayer, M.P. (2012). Structure and Dynamics of the ATP-
1460 Bound Open Conformation of Hsp70 Chaperones. Mol Cell 48, 863–874.
1461 10.1016/j.molcel.2012.09.023.

1462 86. Waterhouse, A., Bertoni, M., Bienert, S., Studer, G., Tauriello, G., Gumienny, R., Heer, F.T.,
1463 De Beer, T.A.P., Rempfer, C., Bordoli, L., et al. (2018). SWISS-MODEL: Homology
1464 modelling of protein structures and complexes. Nucleic Acids Res 46, W296–W303.
1465 10.1093/nar/gky427.

1466 87. Tsai, J., Taylor, R., Chothia, C., and Gerstein, M. (1999). The packing density in proteins:
1467 Standard radii and volumes. J Mol Biol 290, 253–266. 10.1006/jmbi.1999.2829.

1468 88. Alings, F., Sarin, L.P., Fufezan, C., Drexler, H.C.A., and Leidel, S.A. (2015). An evolutionary
1469 approach uncovers a diverse response of tRNA 2-thiolation to elevated temperatures in yeast.
1470 Rna 21, 202–212. 10.1261/rna.048199.114.

1471 89. Sarin, L.P., Kienast, S.D., Leufken, J., Ross, R.L., Dziergowska, A., Debiec, K., Sochacka,
1472 E., Limbach, P.A., Fufezan, C., Drexler, H.C.A., et al. (2018). Nano LC-MS using capillary
1473 columns enables accurate quantification of modified ribonucleosides at low femtomol levels.
1474 Rna 24, 1403–1417. 10.1261/rna.065482.117.

1475 90. Gregorova, P., Sipari, N.H., and Sarin, L.P. (2021). Broad-range RNA modification analysis
1476 of complex biological samples using rapid C18-UPLC-MS. RNA Biol 18, 1382–1389.
1477 10.1080/15476286.2020.1853385.

1478 91. Storey, J.D., and Tibshirani, R. (2003). Statistical significance for genomewide studies. Proc
1479 Natl Acad Sci U S A 100, 9440–9445. 10.1073/pnas.1530509100.

1480 92. Chavali, S., Chavali, P.L., Chalancon, G., De Groot, N.S., Gemayel, R., Latysheva, N.S., Ing-
1481 Simmons, E., Verstrepen, K.J., Balaji, S., and Babu, M.M. (2017). Constraints and
1482 consequences of the emergence of amino acid repeats in eukaryotic proteins. Nat Struct Mol
1483 Biol 24, 765–777. 10.1038/nsmb.3441.

1484 93. Chatr-Aryamontri, A., Breitkreutz, B.J., Heinicke, S., Boucher, L., Winter, A., Stark, C.,
1485 Nixon, J., Ramage, L., Kolas, N., O'Donnell, L., et al. (2013). The BioGRID interaction
1486 database: 2013 Update. Nucleic Acids Res 41, 816–823. 10.1093/nar/gks1158.

1487 94. Benschop, J.J., Brabers, N., van Leenen, D., Bakker, L. V., van Deutekom, H.W.M., van
1488 Berkum, N.L., Apweiler, E., Lijnzaad, P., Holstege, F.C.P., and Kemmeren, P. (2010). A
1489 Consensus of Core Protein Complex Compositions for Saccharomyces cerevisiae. Mol Cell
1490 38, 916–928. 10.1016/j.molcel.2010.06.002.

bioRxiv preprint doi: https://doi.org/10.1101/2023.01.23.524173; this version posted January 23, 2023. The copyright holder for this preprint (which was not certified by peer review) is the author/funder. All rights reserved. No reuse allowed without permission.

1491 95. Liti, G., Carter, D.M., Moses, A.M., Warringer, J., Parts, L., James, S.A., Davey, R.P.,
1492 Roberts, I.N., Burt, A., Koufopanou, V., et al. (2009). Population genomics of domestic and
1493 wild yeasts. Nature 458, 337–341. 10.1038/nature07743.

1494 96. Newman, J.R.S., Ghaemmaghami, S., Ihmels, J., Breslow, D.K., Noble, M., DeRisi, J.L., and
1495 Weissman, J.S. (2006). Single-cell proteomic analysis of S. cerevisiae reveals the architecture
1496 of biological noise. Nature 441, 840–846. 10.1038/nature04785.

1497 97. Arava, Y., Wang, Y., Storey, J.D., Liu, C.L., Brown, P.O., and Herschlag, D. (2003).
1498 Genome-wide analysis of mRNA translation profiles in Saccharomyces cerevisiae. Proc Natl
1499 Acad Sci U S A 100, 3889–3894. 10.1073/pnas.0635171100.

1500 98. Tacutu, R., Thornton, D., Johnson, E., Budovsky, A., Barardo, Di., Craig, T., DIana, E.,
1501 Lehmann, G., Toren, D., Wang, J., et al. (2018). Human Ageing Genomic Resources: New
1502 and updated databases. Nucleic Acids Res 46, D1083–D1090. 10.1093/nar/gkx1042.

1503 99. McCormick, M.A., Delaney, J.R., Tsuchiya, M., Tsuchiyama, S., Shemorry, A., Sim, S.,
1504 Chou, A.C.Z., Ahmed, U., Carr, D., Murakami, C.J., et al. (2015). A Comprehensive Analysis
1505 of Replicative Lifespan in 4,698 Single-Gene Deletion Strains Uncovers Conserved
1506 Mechanisms of Aging. Cell Metab 22, 895–906. 10.1016/j.cmet.2015.09.008.

1507 100. Albu, R.F., Chan, G.T., Zhu, M., Wong, E.T.C., Taghizadeh, F., Hu, X., Mehran, A.E.,
1508 Johnson, J.D., Gsponer, J., and Mayor, T. (2015). A feature analysis of lower solubility
1509 proteins in three eukaryotic systems. J Proteomics 118, 21–38. 10.1016/j.jprot.2014.10.011.

1510 101. Jain, S., Wheeler, J.R., Walters, R.W., Agrawal, A., Barsic, A., and Parker, R. (2016).
1511 ATPase-Modulated Stress Granules Contain a Diverse Proteome and Substructure. Cell 164,
1512 487–498. 10.1016/j.cell.2015.12.038.

1513 102. Giaever, G., Chu, A.M., Ni, L., Connelly, C., Riles, L., Veronneau, S., Dow, S., Lucau-
1514 Danila, A., Anderson, K., Andre, B., et al. (2002). Functional profiling of the Saccharomyces
1515 cerevisiae genome. Nature 418, 387–391. https://doi.org/10.1038/nature00935.

1516

bioRxiv preprint doi: https://doi.org/10.1101/2023.01.23.524173; this version posted January 23, 2023. The copyright holder for this preprint (which was not certified by peer review) is the author/funder. All rights reserved. No reuse allowed without permission.

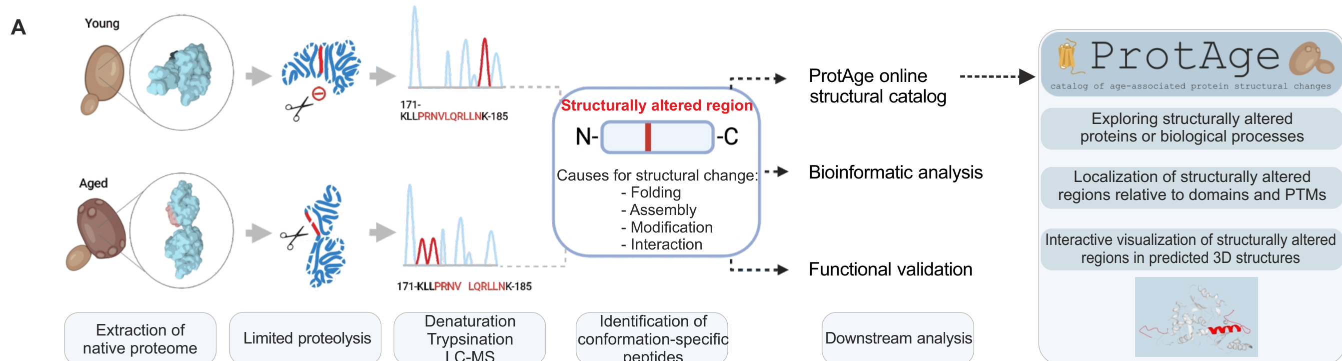

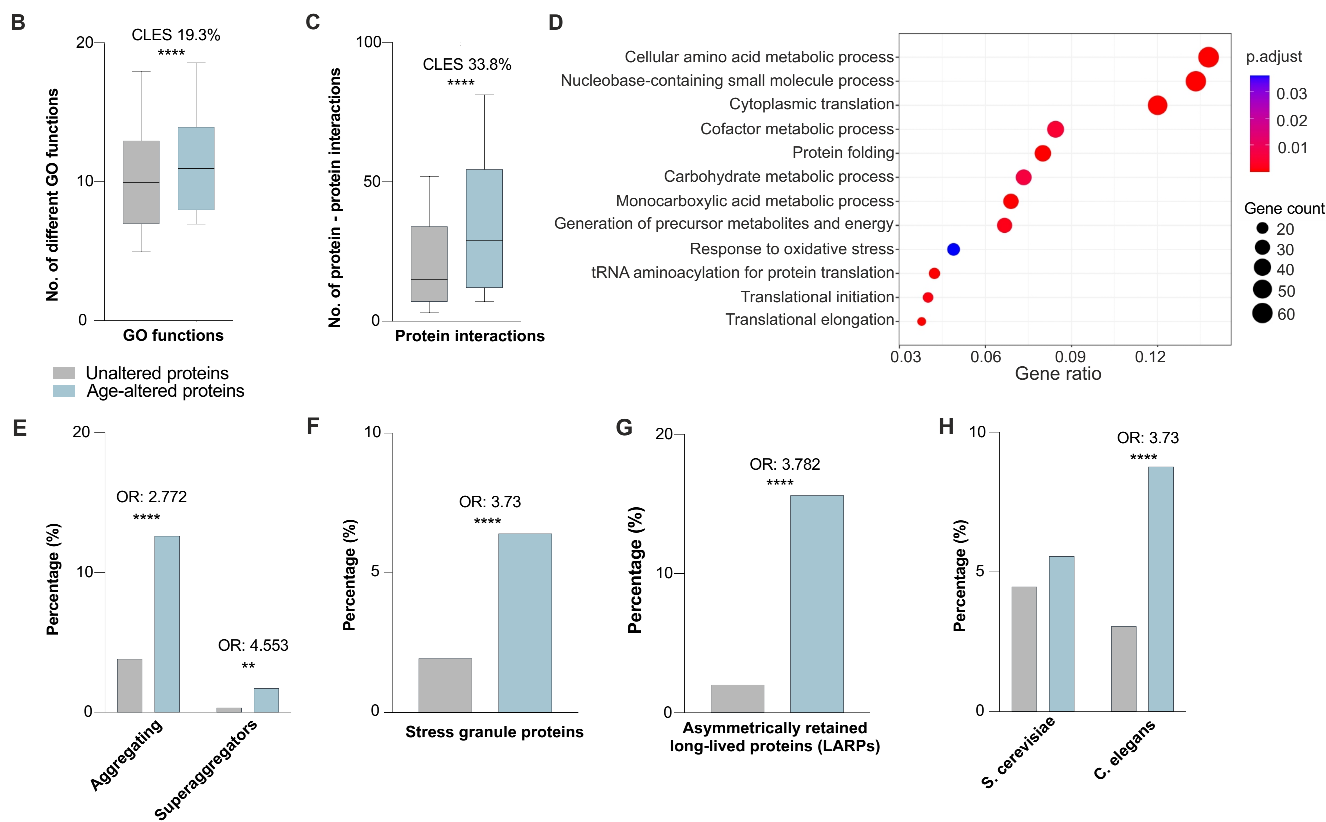

bioRxiv preprint doi: https://doi.org/10.1101/2023.01.23.524173; this version posted January 23, 2023. The copyright holder for this preprint (which was not certified by peer review) is the author/funder. All rights reserved. No reuse allowed without permission.

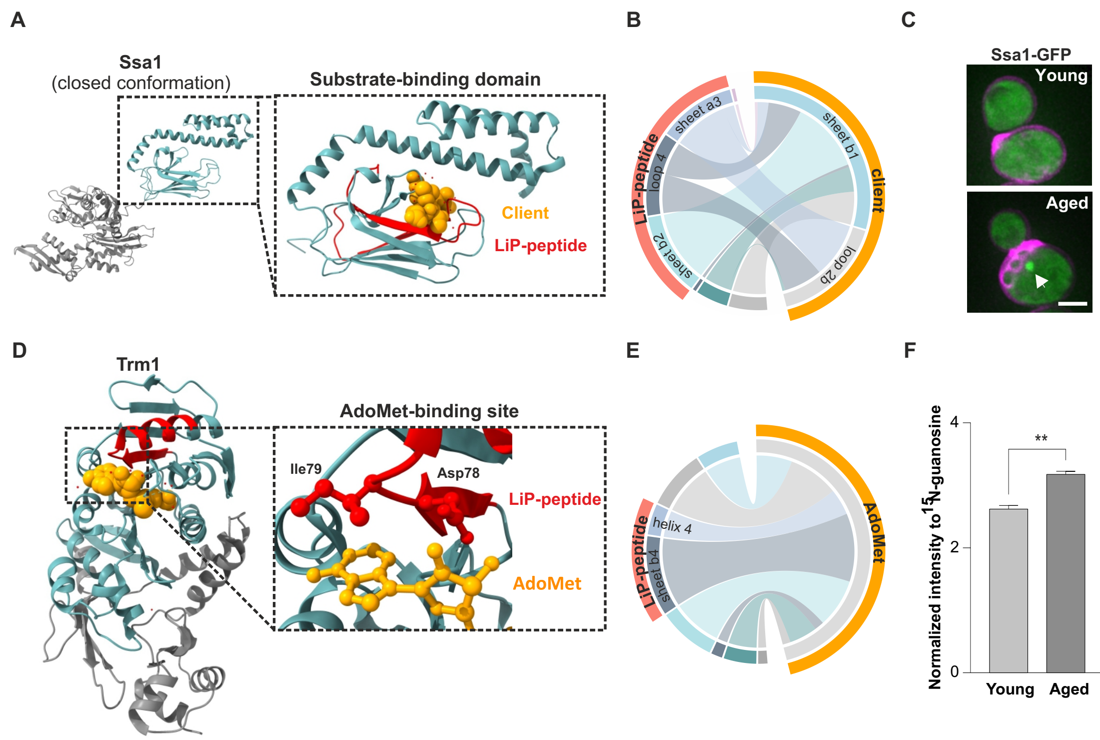

bioRxiv preprint doi: https://doi.org/10.1101/2023.01.23.524173; this version posted January 23, 2023. The copyright holder for this preprint (which was not certified by peer review) is the author/funder. All rights reserved. No reuse allowed without permission.

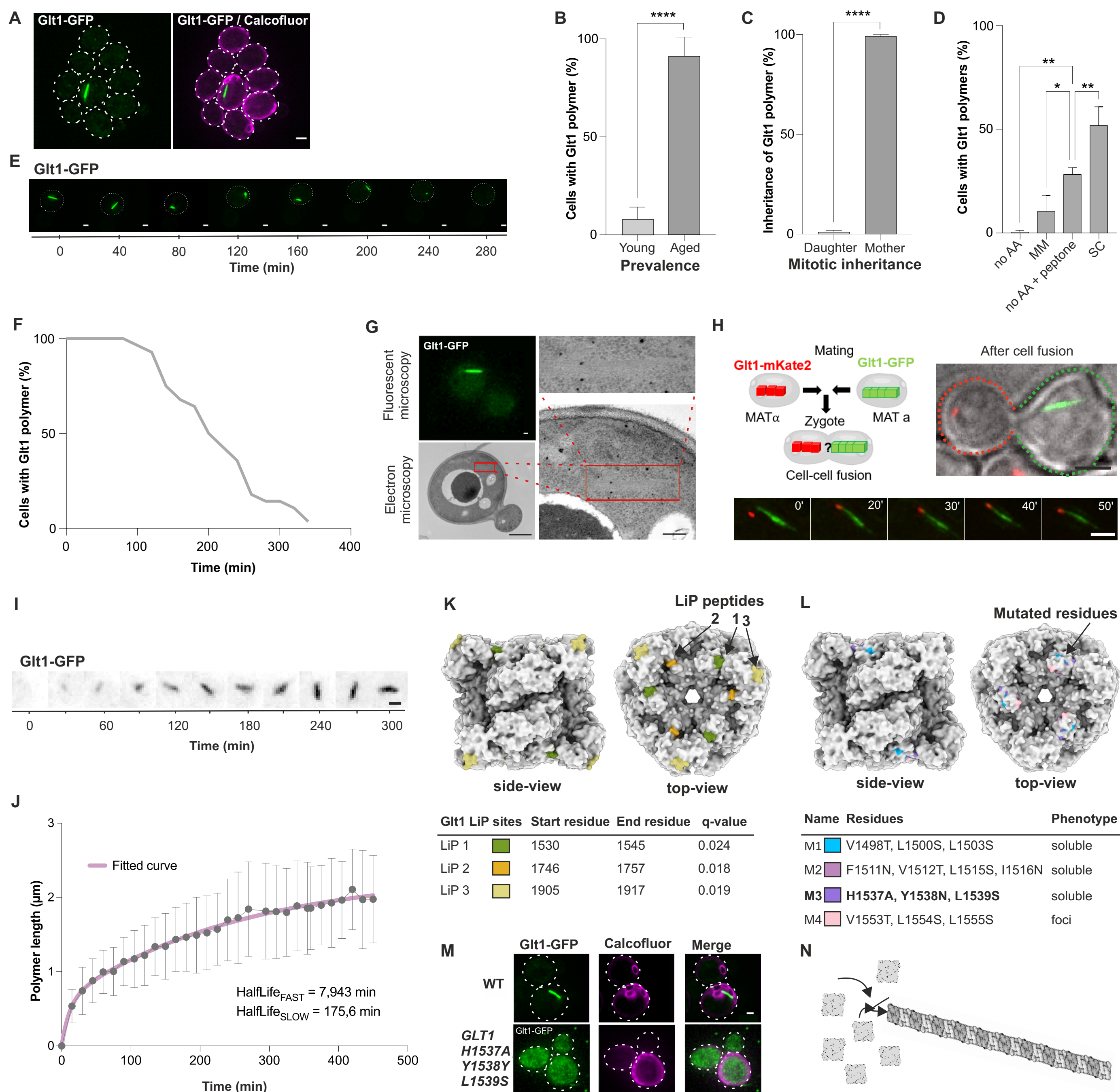

Glt1 LiP sites		Start residue	End residue	q-value
LiP 1	(green)	1530	1545	0.024
LiP 2	(orange)	1746	1757	0.018
LiP 3	(yellow)	1905	1917	0.019

Name	Residues	Phenotype
M1	V1498T, L1500S, L1503S	soluble
M2	F1511N, V1512T, L1515S, I1516N	soluble
M3	**H1537A, Y1538N, L1539S**	soluble
M4	V1553T, L1554S, L1555S	foci

bioRxiv preprint doi: https://doi.org/10.1101/2023.01.23.524173; this version posted January 23, 2023. The copyright holder for this preprint (which was not certified by peer review) is the author/funder. All rights reserved. No reuse allowed without permission.